Assessing Novel Lidar Modalities for Maximizing Coverage of a Spaceborne System through the Use of Diode Lasers

remote sensing

MDPI

Article

Assessing Novel Lidar Modalities for Maximizing Coverage of a Spaceborne System through the Use of Diode Lasers

Johannes N. Hansen [1,*], Steven Hancock [1], Ludwig Prade [2], Gerald M. Bonner [2], Haochang Chen [2], Ian Davenport [1], Brynmor E. Jones [2] and Matthew Purslow [1]

[1] School of GeoSciences, University of Edinburgh, Edinburgh EH8 3FF, UK; steven.hancock@ed.ac.uk (S.H.); ian.davenport@ed.ac.uk (I.D.); matthew.purslow@ed.ac.uk (M.P.)
[2] Fraunhofer Centre for Applied Photonics, Fraunhofer UK Research Ltd., 99 George Street, Glasgow G1 1RD, UK; ludwig.prade@lupra.de (L.P.); gerald.bonner@fraunhofer.co.uk (G.M.B.); haochang.chen@fraunhofer.co.uk (H.C.); brynmor.jones@fraunhofer.co.uk (B.E.J.)
* Correspondence: johannes.hansen@ed.ac.uk

Abstract: Current satellite lidars have sparse spatial coverage, leading to uncertainty from sampling. This complicates robust change detection and does not allow applications that require continuous coverage. One potential way to increase lidar sampling density is to use more efficient lasers. All current spaceborne lidars use solid-state lasers with a limited efficiency of 5–8%. In this paper, we investigate the potential for using diode lasers, with their higher efficiencies, as an alternative. Diode lasers have reported efficiencies of about 25% and are much smaller and lighter than solid-state lasers. However, they can only emit good beam quality at lower peak powers, which has so far prevented them from being used in spaceborne lidar applications. In this paper, we assess whether the novel lidar modalities necessitated by these lower peak powers are suitable for satellite lidar, determined by whether they can match the design performance of GEDI by being able to accurately measure ground elevation through 98% canopy cover, referred to as having "98% beam sensitivity". Through this, we show that a diode laser can be operated in pulse train or pulse compressed lidar (PCL) mode from space, using a photon-counting detector. In the best case scenario, this setup requires a detected energy of $E_{det} = 0.027$ fJ to achieve a beam sensitivity of 98%, which is less than the 0.28 fJ required by a full-waveform solid-state lidar instrument, exemplified by GEDI. When also accounting for the higher laser and detector efficiency, the diode laser in pulse train mode requires similar shot energy as a photon counting solid-state laser such as ICESat-2 which along with the higher laser efficiency could result in a doubling of coverage. We conclude that there is a clear opportunity for diode lasers to be used in spaceborne lidars, potentially allowing wider coverage through their higher efficiencies.

Keywords: lidar; pulse compression; photon counting; diode laser

Citation: Hansen, J.N.; Hancock, S.; Prade, L.; Bonner, G.M.; Chen, H.; Davenport, I.; Jones, B.E.; Purslow, M. Assessing Novel Lidar Modalities for Maximizing Coverage of a Spaceborne System through the Use of Diode Lasers. *Remote Sens.* **2022**, *14*, 2426. https://doi.org/10.3390/rs14102426

Academic Editor: Xuan Zhu

Received: 5 April 2022
Accepted: 13 May 2022
Published: 18 May 2022

1. Introduction

Lidar has been shown to be the optimum technology to measure bare earth elevation beneath vegetation canopies and in complex terrain [1], to measure tree height and to make non-saturating measurements of aboveground biomass [2]. Recent years have seen a number of lidar satellites launched, all of which are collecting unique data. These include the Ice, Cloud and land Elevation Satellite 2 (ICESat-2) mission [3], optimized to measure ice elevation, and the Global Ecosystem Dynamics Investigation (GEDI) mission [2], optimized to measure forest structure. These provide near global coverage, allowing consistency and lower cost per unit area than Airborne Laser Scanning (ALS). This makes them the ideal technology for mapping global vegetation structure [2,4,5].

However, the energy requirements of lidar result in limited spatial and temporal coverage compared to passive-optical and radar satellites, with even the densest sampling satellite lidar, GEDI, only directly imaging 2–4% of the Earth's surface once during its mission lifetime [2]. This sparse sampling means that multiple years of data need to be

combined to produce a single global map, and adds uncertainty to the estimate [6]. The sampling uncertainty and limited temporal coverage limits their use in robust change detection, something currently limiting the certainty in global carbon modelling [7].

One proposal to overcome this sparse sampling is to use the available lidar data to calibrate another continuous dataset such as passive-optical [8], radar [9,10] or a fusion of the two [11]. This approach has underpinned a number of global biomass maps [12–14]. However, some field comparison studies suggest that the uncertainties are being underestimated [15], whilst some studies suggest that overfitting of the calibration models may be leading to overly optimistic accuracy assessments [16]. These questions currently prevent such fused products from being used for robust change detection.

Hancock et al. [17] showed that satellite lidar could achieve regularly updated, continuous coverage by launching a constellation of 12 ICESat-2-sized satellites, allowing change detection without the issues described above and being suitable for applications that require continuous coverage such as flood modelling. This would be prohibitively expensive; so technological developments are needed to increase the coverage of satellite lidar per unit cost. This paper explores the use of alternative laser sources, and the novel lidar modalities they require, to achieve accurate ground elevation measurements through 98% canopy cover (referred to as "98% beam sensitivity"), and whether they can achieve this with a lower satellite power requirement than a solid-state laser.

2. Lidar Coverage

The coverage of a satellite lidar is controlled by the swath width, s. This can be given as a function of the properties of the lidar satellite and data products [17]:

$$s = \frac{P_{\text{pay}} L_{\text{e}}}{E_{\text{det}}} \frac{A}{2\pi h^2} Q \rho \tau^2 \frac{r^2 (R+h)^{\frac{3}{2}}}{R\sqrt{GM}} \quad (1)$$

where P_{pay} is the satellite payload power, L_{e} is the laser electric-to-optical efficiency (including cooling), E_{det} is the minimum detected energy per laser shot needed for an accurate measurement (related to signal-to-noise-ratio), A is the telescope area, h is the satellite altitude, Q is the detector efficiency (quantum efficiency for a waveform detector or single photon detection efficiency for photon counting), ρ is the surface reflectance, τ is the atmospheric transmittance, r is the data product spatial resolution, R is the radius of the Earth, M is the mass of the Earth, and G is the gravitational constant.

The swath width can be used within an orbital simulation tool to determine how many satellites are needed to have a certain probability of measuring the whole Earth within a given time frame [17], which can then be multiplied by the cost per satellite to estimate the total constellation cost. Thus, the total system cost is inversely proportional to s; so increasing the numerators or decreasing the denominators in Equation (1) leads to a reduction in system cost.

The parameters in Equation (1) are controlled by the satellite platform (P_{pay}, A, h), by the environmental conditions (τ, ρ) and by the data product properties (r). Some are universal constants (G, M, R), and the rest are controlled by the lidar instrument. This paper concentrates on the parameters controlled by the lidar instrument photonics and signal processing. Those are:

- L_{e}—controlled by the laser source;
- Q—controlled by the detector;
- E_{det}—controlled by the signal processing method and noise level.

This paper explores methods to increase L_{e} by making use of the alternative laser sources described in Section 2.2. The laser sources considered require different lidar modalities to perform satellite remote sensing due to their much lower peak power limits than currently in-orbit solid-state lasers, which then result in different values for E_{det}. These are described in Section 2.3. The different lidar modalities also have different detector requirements, described in Section 2.4.

The number of satellites required to achieve global coverage in a time period T_{repeat} has been derived by Hancock et al. [17] as

$$N_{\text{sat}} = \left\lceil \frac{c_\delta T_{\text{repeat}}}{s T_{\text{orbit}}} \frac{\ln(1 - p_{\text{obs}})}{\ln(c_{\text{frac}})} \right\rceil \tag{2}$$

where c_δ is the Earth's circumference at latitude δ, s is the swath width of a single satellite (given by Equation (1)), T_{repeat} is the time period in which global coverage is achieved, T_{orbit} is the duration of a single orbit, p_{obs} is the required probability of obtaining a valid observation, and c_{frac} is the cloud cover fraction.

A lower required energy E_{det} leads to a larger swath width s and a lower number of satellites N_{sat} for a given payload power per satellite. The number of required satellites is also a direct driver of system cost. We will use the number of satellites required to achieve complete coverage at the equator in $T_{\text{repeat}} = 5\,\text{yr}$ as the metric to compare different lidar modalities. We assume a mean cloud cover of $c_{\text{frac}} = 0.55$ [17] and set a minimum probability of cloud-free observation of $p_{\text{obs}} = 0.8$.

The achievable swath width and satellite numbers for solid-state and diode lasers under different lidar modalities will be explored and used to inform the choice of technology for a future global lidar system mission.

2.1. Laser Requirements

There is a requirement on the minimum horizontal and vertical accuracy for the measurements to be useful from a scientific perspective, and these have been clearly defined by the GEDI mission [2]. The horizontal resolution is dictated by the size of the laser beam footprint on the ground. This should be no more than 30 m in diameter to avoid slope effects such as topographic blurring [18,19]. Furthermore, the signal-to-noise ratio (SNR) of the ground return must be sufficient to be able to accurately measure ground elevation under dense canopy (root mean square error less than 4 m). In particular, the requirement is a 98% beam sensitivity—i.e., a 90% chance of detecting the ground under 98% canopy cover [2], which is required to accurately determine the ground elevation, which in turn is required to accurately determine the heights and profiles of targets aboveground. The concept of beam sensitivity is explained in Hancock et al. [20], and further details are given in Section 3.3. Finally, to clearly distinguish the ground from the canopy and understory, the pulse must be able to resolve targets that are no more than 5 m apart [2]. This puts a limit on the maximum pulse width [21]. Note that the ground elevation accuracy is not directly related to the pulse width and can be much finer than the range resolution [21], but if the pulse width is too long, the ground and canopy cannot be separated, and bias will be introduced [22]. Because of the geometry of the lidar measurement, the emitted pulse must travel twice the distance between source and target, and the range is calculated as one half the travel time. The *effective* pulse width is therefore one half the pulse width emitted by the laser. Unless explicitly stated otherwise, all pulse widths, lengths, and frequencies stated throughout this paper are the properties of the effective (frequency doubled) rather than the emitted pulse. Figure 1 shows how a sample profile is seen by lidars with effective pulse widths of 15 ns and 30 ns (full-width half maximum (FWHM)). The longer pulse is unable to resolve the ground in this example, and the detected ground would be placed at the lowest peak which is now several meters above the true ground.

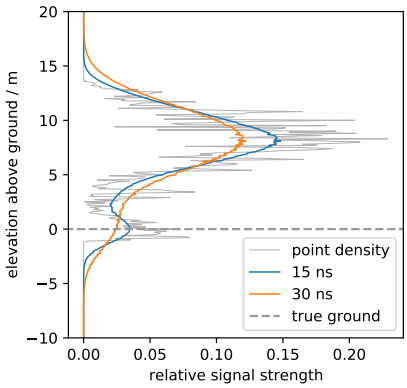

Figure 1. This figure illustrates the effect of the pulse width on the measured return waveform (grey). While short pulses (15 ns shown in blue) can resolve the ground (shown as a dashed line) in this case, wider pulses (30 ns shown in orange) can no longer resolve close details, and the ground signal is lost.

2.2. Laser Sources

All current satellite lidars, outlined in Table 1, have used Q-switched solid-state lasers. The GEDI, ICESat, CALIPSO, Aeolus and LITE lidars all used Nd:YAG lasers [2,23–27], and ICESat-2 and CATS use a Nd:YVO_4 laser [3]. These are 5 to 8% efficient [28,29], although the highest end, 8% for GEDI, was achieved by external cooling on the International Space Station. The highest efficiency lidar to include its own cooling is ICESat-2 at 5%. However, efficiencies of up to 11% have been reported for Yb:YAG solid-state lasers [30] (although not yet flown in space). If the efficiency can be raised without increasing cost, the coverage of spaceborne lidar per unit cost can be increased. As can be seen from the table, these systems give very high energies in single short pulses (typically a few nanoseconds or tens of nanoseconds), resulting in peak powers of many hundreds of kilowatts.

Table 1. This table shows current and past operational spaceborne lidars and their properties. Note that the LITE technology demonstrator is not included. All of these are based on solid-state laser sources, mainly Nd:YAG.

Instrument	Pulse Rate (Hz)	E_{shot} (mJ)	Number Tracks	P_{avg} (W)	P_{peak} (kW)	λ (nm)	Detector type [a]	D [b] (cm)	H [c] (km)	In Orbit
ICESat	40	100	1	4.0	8300	1064, 532	FW	80	600	2003–2009
CALIPSO	20	110	1	2.2	2750	1064, 532	FW	100	705	2006–
CATS	10,000/5000	1–2	3	15.0		1064, 532, 355	PC	60	400	2015–2017
Aeolus	51	110	1	5.6	2750	355	FW	150	320	2018–
ICESat-2	10,000	1.2	6	12.0	400	532	PC	80	481	2018–
GEDI	242	10	8	7.3	320	1064	FW	80	420	2018–

[a] FW—full waveform, PC—photon counting; [b] telescope diameter; [c] altitude.

A potential alternative to these is provided by diode lasers. These have higher efficiencies than solid-state lasers at around 25%. This efficiency combines the diode laser efficiency itself, which is typically around 50% [31] (p. 15), with the energy loss from thermo-electric cooling (TEC) which is also typically around 50% (see, for example, [32]), which under most conditions puts out waste heat (corresponding to the total power consumed) of about double the heat removed from the object being cooled. As no diode lasers have been flown in space, we will consider the best current R&D performance for both types of lasers, i.e., 11% for solid-state lasers and 25% for diode lasers. Additionally, diode lasers are smaller in volume and mass than solid-state lasers (which themselves typically include a diode laser as the pump source, plus many other components) and are simpler to engineer for resilience against shock and vibration. For that reason, while the diode lasers considered

here have not yet flown in space, only relatively modest engineering changes would be required to raise their technology readiness level (TRL). The solid-state laser described in [30], also not yet flown, is therefore considered a reasonable point of comparison.

However, unlike solid-state lasers, diode lasers cannot be Q-switched to achieve high pulse energies/peak powers due to the short upper-state lifetime of the semiconductor gain material. Therefore, while diode lasers can be pulsed very quickly, the peak power is typically close to the average power limit in Continuous Wave (CW) operation, unlike solid-state lasers where peak powers for Q-switched pulses can be many orders of magnitude greater than the CW average power limit. Diode lasers can achieve average powers on the order of a few kilowatts, but such systems are based on stacks of multiple diode bars resulting in poor spatial beam quality which renders such systems unsuitable for satellite lidar as it would significantly increase the footprint size on the ground.

Therefore, for purposes of satellite lidar, we must look at classes of diode lasers that offer good beam quality and moderate powers, namely those with tapered semiconductor structures. Such tapered lasers tend to have average (and hence peak) power limits of around 5 W, although manufacturers are continuing to push these limits slowly upwards, [31] (slide 15), and it may be possible to achieve peak powers several times the CW damage threshold by overdriving the diode laser for only very short periods of time [33]. Nonetheless, peak powers available from diode lasers with good beam quality are still many orders of magnitude lower than those offered by solid-state lasers. As a consequence, emitting sufficient energy for an accurate measurement from space would take milliseconds. Therefore, standard lidar signal processing techniques such as Gaussian decomposition [21] would not allow the accurate measurement of ground elevation or vegetation To perform lidar remote sensing with diode lasers, alternative lidar modalities are needed.

2.3. Lidar Modalities

2.3.1. Single Pulse

Traditional satellite lidars emit a single pulse of light towards the ground and record the returned energy as a function of range to produce a lidar waveform. This can be performed either with a full-waveform detector, as used on GEDI [2], or by counting individual return photons on a photon-counting detector and then aggregating to make a pseudo-waveform, as used in ICESat-2 vegetation products [34]. This is referred to in this paper as single pulse lidar modality. As stated above, it requires peak powers of hundreds of kilowatts and can only be achieved by solid-state lasers. As diode lasers cannot achieve these peak powers, alternative modalities must be used. A sample pulse is illustrated in Figure 2.

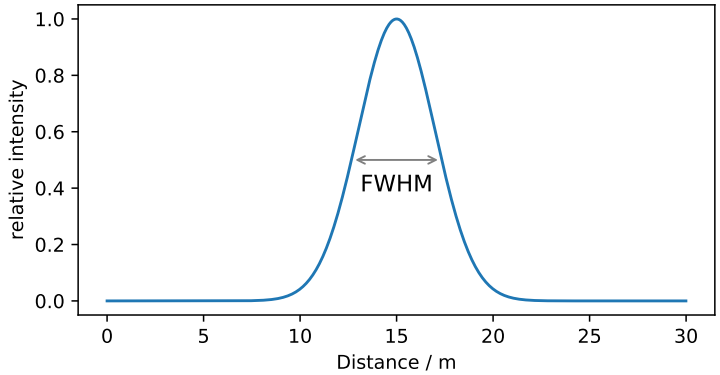

Figure 2. Illustration of a standard Gaussian pulse as emitted by a solid-state laser. The pulse shown here has a FWHM of 15.6 ns, corresponding to $\sigma \approx 2$ m. The peak power is 320 kW for a 10 mJ pulse.

2.3.2. Pulse-Train

One potential approach is to emit many short pulses in a sequence, each short enough to allow the required range resolution ($\leq 5\,\mathrm{m}$) but not exceeding the peak power limits, and then aggregate all returns to produce a pseudo-waveform. This is referred to as a pulse train and is illustrated in Figure 3.

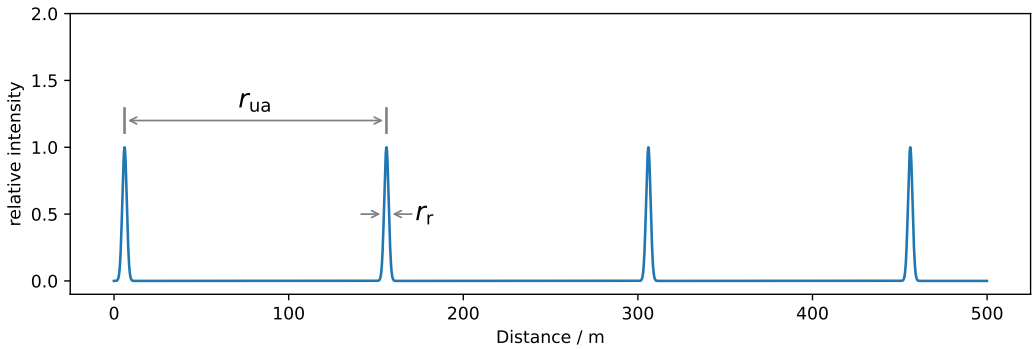

Figure 3. Illustration of a pulse train with an unambiguous range of $r_{ua} = 150\,\mathrm{m}$ and a range resolution of $r_r = 3\,\mathrm{m}$. Four repetitions are shown. In practice the number of repetitions will be about 4000.

The pulse train is characterized by the individual pulse width, the distance between pulses and the number of repetitions. The pulse width determines the range resolution r_r, while the distance between consecutive pulses determines the maximum unambiguous range r_{ua}, i.e., the maximum vertical distance that targets can be apart while being unambiguously attributable to their respective pulse. This should be set to more than the largest vertical distance between targets on the ground, i.e., at least the maximum expected canopy height (roughly 100 m for the tallest tree on Earth).

The maximum possible number of repetitions is determined by the dwell time and the unambiguous range:

$$N_{rep} = \frac{cT_{dwell}}{2r_{ua}} \tag{3}$$

For $T_{dwell} = 4\,\mathrm{ms}$ and $r_{ua} = 150\,\mathrm{m}$, this gives 4000 repetitions. During this time, any noise from background light or electronics will be integrated, making the noise effectively 4000 times the noise for a single pulse system.

2.3.3. Pulse Compressed Lidar (PCL)

Another technique with the potential to enable lidar remote sensing with a diode laser is Pulse Compressed Lidar (PCL). PCL distributes the energy across the length of a longer pulse (microseconds rather than nanoseconds long), giving a low peak intensity but with a particular pulse shape or modulation pattern. This allows sufficient energy to be emitted without exceeding the diode's peak power limits. For a full-waveform lidar, a pulse microseconds long would result in a range resolution too coarse for lidar remote sensing. The pulse shape is specifically chosen to allow for signal reconstruction via cross-correlation of the return waveform with the emitted pulse shape. In particular, this requires that the autocorrelation of the pulse shape with a shifted version of itself is zero, allowing for a perfect reconstruction of the signal in theory. The maximum possible resolution of the restored signal is limited by the bandwidth of frequencies present in the emitted pulse (this can be approximated to the peak frequency in most cases).

Frequency Chirps

One type of pulse used in PCL is a frequency chirp [35]. This is a sine wave whose frequency is gradually ramped up (or down) from the start to the stop frequency.

The chirped pulse is given by the following equation:

$$y(t) = \sin\left(2\pi\left(\frac{ct^2}{2L}(f_{\text{stop}} - f_{\text{start}}) + tf_{\text{start}}\right)\right) \quad (4)$$

where L is the sweep distance (e.g., 100 m), c is the speed of light and f_{start} and f_{stop} are the start and stop frequencies of the frequency sweep. Example chirps with a start frequency of 1 MHz and peak frequencies of 100 MHz, 600 MHz, and 2 GHz are shown in Figure 4.

These chirps need to be sampled at a minimum of twice the peak frequency (Nyquist frequency) to avoid aliasing. For this reason, higher peak frequencies require denser sampling, resulting in a higher number of bins and a lower number of photons per bin, potentially making higher frequencies less robust to noise.

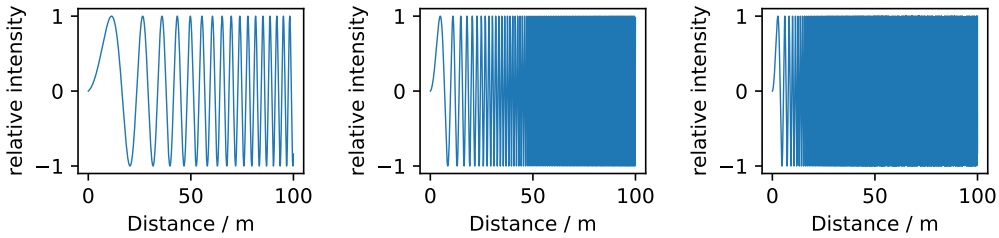

(**a**) Chirp (100 MHz) (**b**) Chirp (600 MHz) (**c**) Chirp (2000 MHz)

Figure 4. This figure shows three examples of chirped pulses with linear frequency sweeps from 1 MHz to 100 MHz (**a**); 600 MHz (**b**); and 2 GHz (**c**). Chirps are used to maintain high range resolution even at longer pulse lengths.

Other Pulse Shapes

It is possible to use PCL with other pulse shapes. One alternative to frequency chirps is Maximum Length Sequences, which are generated using a linear feedback shift register. Their autocorrelation function is a Kronecker delta [36]. Another option are Zadoff–Chu sequences which have similar autocorrelation properties [37,38]. While these pulse shapes are designed specifically for optimal signal reconstruction via cross-correlation, our initial trials suggest a poor performance in the photon counting case. Our analysis is therefore focused on frequency chirps.

2.3.4. Phase-Based

Another technique to lower the peak power requirements is phase-based lidar. This modulates the outgoing laser intensity with multiple frequencies (typically 3) and then combines that with the return intensity. The phase shift between the output and return is used to determine the range to a single target per laser footprint. Whilst this technique is common for terrestrial lidar in artificial environments where the very small footprint (typically millimetres) means that it is safe to assume that each laser shot hits only a single target, it cannot retrieve multiple returns per shot. It is therefore unsuitable for use in vegetated environments [39] or with large footprints. For this reason, phase-based lidar will not be considered for use here.

2.4. Detectors

This paper considers two types of detectors, full-waveform [2] and photon counting [3]. Both have been used on satellite lidars, with full-waveform detectors on ICESat, GEDI, CALIPSO and Aeolus and photon-counting detectors on CATS and ICESat-2. Whilst photon-counting detectors such as single photon avalanche diodes (SPADs) and silicon photomultipliers (SiPMs) have several advantages such as a higher sensitivity in a low-light environment, lower dark count noise and no electronic noise of circuits and analog-to-digital converters (ADCs), and thus potentially allow for higher SNRs for the same signal energy, these detectors are subject to a so-called dead time [40]. The dead time refers to the

time it takes for the detector element to be reset after detecting a photon before it can detect another. During that reset time (typically tens of nanoseconds), the detector is effectively blind to new photons. This leads to distortions that prevent accurate measurements and makes the detector easier to saturate, inducing a first photon bias [40]. Full-waveform detectors remain sensitive to all photons that arrive at the detector, although at the expense of greater electronic noise. For this reason, only full-waveform detectors have been used so far for detecting the ground through dense forests.

Both photon counting and full-waveform detectors are made from similar semiconductor materials and have a quantum efficiency of around 45% [28,41] (probability of a photon hitting a detector element being recorded as an electrical signal). However, photon-counting detectors can have an additional penalty to avoid distortions from dead time. The risk of dead-time-induced distortions on photon counting systems can be avoided in one of two ways: (1) by using low photon rates to reduce the chance of two photons arriving within the dead time, (2) by using an array of detector elements to reduce the chance of two photons hitting the same detector element within the dead time, or some combination of the two. For systems with photon rates so low that there is a low probability of two photons arriving within the dead time, a single detector element can be used, and the detector can have a photon detection efficiency (PDE) of the quantum efficiency. When systems require multiple detector elements to reduce dead time, the pixel elements cannot be packed together perfectly due to the need for the pixel electronics. The fraction of the detector array made up of the detecting pixels (rather than the supporting electronics) is known as the fill-factor and introduces an additional photon loss.

As an example, ICESat-2 is expected to have a signal photon rate of 10 photons per shot over ice and only 1–2 photons per shot over forest [3]. To allow 10 photons to be detected without a dead time, it has a 4×4-element detector with a fill-factor of 33%, resulting in a PDE of 15% (product of quantum efficiency and fill-factor) [41]. In our case, the shot energy of a comparable system would need to be increased to detect a ground signal through dense canopy. The number of signal photons would then be high enough even over forest to require a multi-element detector. A similar PDE of 14.2% at 500 nm with a high fill-factor of 42.4% has been demonstrated in [42]. With the rapid development of photon-counting detectors and the growing demand for lidar technology, the performance of SPAD arrays has been improving in recent years. In 2020, a SPAD array with 31.4% PDE at 850 nm with 3 V excess bias was reported [43]. A SPAD array with over 100,000 pixels, 29% PDE at 850 nm, 22% PDE at 905 nm and only 6 ns dead time was published in 2021 by Sony [44]. The timing modules and data processor are also integrated with the SPAD array into a compact CMOS chip. Considering there is no need for that many pixels in this remote sensing application, the PDE of this SPAD array has the potential for further improvement. For single-element detectors, a PDE of up to 58% at 850 nm has been claimed by Excelitas [45].

Throughout this paper, we use Q to denote the overall PDE, including quantum efficiency and fill-factor. For our analysis, we assume a detector efficiency of $Q = 58\%$ for full-waveform or single-detector element photon counting systems and $Q = 31\%$ for photon counting systems that need to record multiple photons per laser shot. These correspond to the efficiency of currently available best-in-class components at 850 nm.

2.5. Estimation of Noise Photons

As the beam sensitivity is a measure of the signal-to-noise ratio, it is determined not only by the number of signal photons, but also the number of noise photons that are detected in the same period. It is therefore essential to estimate the expected rate of background photons as accurately as possible.

2.5.1. Lunar Noise

To minimize the number of background photons from solar radiation, the mission is intended to be flown at night (in a terminator orbit) such that there is only lunar back-

ground light to consider. For the full moon, a lunar surface radiation with a magnitude 4×10^{-5} that of solar, an instrument filter width of 30 pm, moon at zenith, a satellite altitude of 481 km and a circular telescope diameter of 0.8 m, then the lunar illumination is 6.6×10^{-6} photons μs^{-1} for a wavelength of 850 nm (7.1×10^{-6} photons μs^{-1} for 1064 nm) and will scale proportionally to the field-of-view, bandpass filter width and telescope area, and inversely with the square of satellite altitude. Total noise counts will then be the product of this and the integration time.

$$n_{\text{lunar,ICE}} = 6.6 \times 10^{-6} \text{ photons } \mu s^{-1}$$

2.5.2. Dark Count

Dark count, the noise inherent in the detector without illumination, was measured by the ICESat-2 ATLAS instrument with the laser off and the door closed in the range of 4×10^{-4} photons μs^{-1} to 8×10^{-4} photons μs^{-1} [41], excluding the area covered by the South Atlantic anomaly where counts peak at 0.02 photons μs^{-1}. The dark count is partially due to charged particles triggering the detector, and it is higher in northern latitudes. This is independent of any emitting laser characteristics but may change with detector technology such as the cross-sectional area of the sensor. For single element detectors, a widely used commercial SPAD (the MPD's PDM series) is able to provide a dark count rate (DCR) of <50 cps (counts per second) [46]. For large-scale array detectors, a 192 × 128 CMOS SPAD array with 25 cps median DCR/pixel has been reported in 2019 [47]. These values are much smaller than the rates recorded on ICESat-2. However, they are measured in a laboratory environment shielded from the influence of cosmic rays. We therefore take the ICESat-2 rate as a more realistic value for a spaceborne detector.

$$n_{\text{dark,ICE}} = 8 \times 10^{-4} \text{ photons } \mu s^{-1}$$

2.5.3. Atmospheric Scattering

The total background noise rate measured by ICESat-2 ATLAS at night was measured from the 22×10^6 14 km-length atmospheric profile observations from returns bounded by the north and south poles and 2.8° W, 2.8° E longitude where the sun was at least 30° below the horizon. This produced a mean noise of 0.012 μs^{-1} with a standard deviation of 0.017 μs^{-1}. This is over an order of magnitude larger than the dark count, three orders of magnitude larger than the estimated lunar noise and is highly variable. We therefore hypothesize that this is predominantly due to backscattering of ICESat-2's ATLAS laser from the atmosphere and aerosols. To test this hypothesis, we extracted the number of noise photons per ATLAS shot, which came to 0.115 noise photons per strong shot over 7.22 µs and 0.046 per weak shot over 7.34 µs. The dependence on beam power suggests that these are signal photons being backscattered from the atmosphere at a rate of about 0.077 photons mJ^{-1}. We are assuming that this absorption is proportional to the atmosphere's optical depth, which at ATLAS's 532 nm is about 0.38 (calculated as an average over scenarios using MODTRAN), at 850 nm is about 0.16 and at 1064 nm is about 0.12. In particular, this noise contribution is independent of the specific detector and laser source used and only depends on the wavelength in the way described here. It is therefore appropriate to use measurements from ICESat-2 to calculate the expected atmospheric scattering noise.

$$n_{\text{atm,ICE}} = 0.077 \text{ photons } mJ^{-1}$$

2.5.4. Total Noise Rate

To adapt the ICESat-2 noise rates for a system with different parameters, each of these noise components need to be scaled as follows:

1. The lunar noise (n_{lunar}) is proportional to h^{-2}, $\Delta\lambda$, A, and Q.
2. The dark count (n_{dark}) is constant and does not scale with any of the parameters.
3. The atmospheric scattering (n_{atm}) scales with σ_λ, A and Q.

The individual components are therefore:

$$n_{\text{lunar}} = n_{\text{lunar,ICE}} \frac{h_{\text{ICE}}^2}{h^2} \frac{\Delta\lambda}{\Delta\lambda_{\text{ICE}}} \frac{Q}{Q_{\text{ICE}}} \frac{\sigma_\lambda}{\sigma_{\text{ICE}}} \frac{A}{A_{\text{ICE}}} \tag{5}$$

$$n_{\text{dark}} = n_{\text{dark,ICE}} \tag{6}$$

$$n_{\text{atm}} = n_{\text{atm,ICE}} \frac{Q}{Q_{\text{ICE}}} \frac{\sigma_\lambda}{\sigma_{\text{ICE}}} \frac{A}{A_{\text{ICE}}} \tag{7}$$

Here, $\Delta\lambda_{\text{ICE}} = 30\,\text{pm}$ is the bandpass filter width of ICESat-2, λ is the wavelength of the proposed instrument, σ_{ICE} is the atmospheric optical depth at the wavelength used by ICESat-2, σ_λ is the atmospheric optical depth at the proposed instrument wavelength, $Q_{\text{ICE}} = 0.15$ is the detector efficiency of ICESat-2, $A_{\text{ICE}} = 0.5\,\text{m}^2$ is the telescope area of ICESat-2 and $E_{\text{shot,ICE}} = 1.2\,\text{mJ}$ is the shot energy of the ICESat-2 laser instrument.

The lunar background and dark count are rates of noise photons per time and must be multiplied by the total integration time T to give the total number noise photons. The atmospheric scattering noise only depends on the total laser energy E_{shot} emitted but not on T. The total noise is then calculated as:

$$N_{\text{noise}} = (n_{\text{lunar}} + n_{\text{dark}})T + n_{\text{atm}} E_{\text{shot}} \tag{8}$$

Table 2 lists the resulting noise rates for the three lidar modalities introduced in Section 2.3. As well as the longer integration time, diode lasers have less stable wavelengths than solid-state and so require wider bandpass filters to avoid losing laser energy. The total number of noise photons will then depend on the integration time T and the laser energy E_{shot}.

Table 2. This table shows a summary of the expected noise photon rates and the total noise photon counts for the three lidar modalities introduced in Section 2.3 at a wavelength of 850 nm. The noise rate depends on the detector efficiency Q, the bandpass filter width $\Delta\lambda$, the telescope area A and the detector integration time, which itself depends on the number of pulse repetitions.

Laser Source:	**Solid-State**	**Diode**	
Lidar Modality:	**Single Pulse**	**Pulse Train**	**PCL**
Q	0.31	0.58	0.58
$\Delta\lambda$	30 pm	1 nm	1 nm
N_{rep}	1	4000	4000
Integration time	1 µs	4 ms	4 ms
Noise rate/µs^{-1}	8.1×10^{-4}	1.32×10^{-3}	1.32×10^{-3}
Noise rate/mJ^{-1}	0.067	0.125	0.125

Figure 5 shows the resulting number of expected noise photons as a function of the number of signal photons (as a proxy for E_{shot}). The noise varies with the laser wavelength because of the photon energy and differing optical depth of the atmosphere. The figure therefore shows the noise rates for three wavelengths: 532 nm (ICESat-2), 850 nm (the proposed wavelength for a diode laser instrument) and 1064 nm (GEDI). The numbers shown are for a 4 ms integration time, i.e., the pulse train or PCL modalities.

The lines are calculated from Equation (8) with the constant offset corresponding to the lunar background Equation (5) and dark count Equation (6). The gradient of the lines, i.e., the energy dependent component, is driven by atmospheric scattering and varies with the optical depth of the atmosphere for different wavelengths.

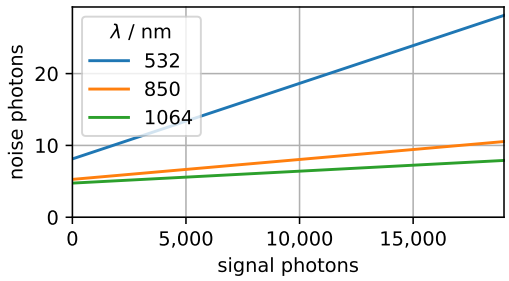

Figure 5. This figure shows the total number of noise photons for an integration time of 4 ms as a function of the number of signal photons as calculated from Equation (8) for three different laser wavelengths. The noise is made up of lunar background, dark count and atmospheric scattering. The resulting equations are: $N = 2.03 \times 10^{-3}\,\mu s^{-1} T + 0.298\,mJ^{-1} E_{shot}$ for 532 nm, $N = 1.32 \times 10^{-3}\,\mu s^{-1} T + 0.125\,mJ^{-1} E_{shot}$ for 850 nm, $N = 1.19 \times 10^{-3}\,\mu s^{-1} T + 0.094\,mJ^{-1} E_{shot}$ for 1064 nm.

While background noise is an experimental factor that can potentially be reduced by careful selection of the laser wavelength, optical bandpass filters and other means, there is an additional source of noise called shot noise. Shot noise is an intrinsic property of the discrete nature of light and results in additive noise that follows a Poisson distribution with a standard deviation of $\sqrt{N}$. For large N, it can be approximated by a Gaussian distribution.

2.6. Energy and Power Estimation

The detected energy E_{det} is directly proportional to the number of detected photons $N_{photons}$:

$$E_{det} = h\frac{c}{\lambda}N_{photons} \tag{9}$$

where h is the Planck constant, c is the speed of light, and λ is the wavelength. The shot energy E_{shot} that must be emitted to detect an energy E_{det} depends on the detector efficiency Q, the satellite altitude h, the telescope area A, the surface reflectance ρ and the atmospheric transmittance τ:

$$E_{shot} = \frac{E_{det}}{Q}\frac{2\pi h^2}{A}\frac{1}{\rho\tau^2} \tag{10}$$

The average power P_{avg} and the peak power P_{peak} are calculated as described in Appendix A.

3. Methods

All results for this paper were obtained from simulations taking several dense Airborne Laser Scanning (ALS) datasets as input and producing the expected waveforms from a spaceborne instrument as output.

3.1. Lidar Simulator

A satellite lidar simulator was originally developed for the ESA A-Scope mission [22] and subsequently improved for the NASA GEDI mission [20] following the method of Blair and Hofton [48]. This has already been used to simulate traditional waveform lidars and photon counting systems [11]. The simulator is driven by high-resolution point clouds collected from ALS data and applies the spaceborne lidar footprint shape, pulse shape, detector response and signal and noise level to create a synthetic lidar signal. Signal processing algorithms can be applied to these synthetic lidar signals to extract measurements in the same way as real spaceborne lidar data, allowing the calibration of satellite data [11,49] and explorations of the accuracies of future missions [4]. The accuracy of the simulator has been validated, both in terms of retrieved metric values and in terms of retrieved metric accuracy as a function of beam sensitivity [20]. We used this simulator to quantify the performance of a spaceborne lidar with photon counting and PCL (photon-PCL). The simulator can be used with any laser pulse shape, including the chirped

pulse used in PCL. The only new modifications needed were to add the cross-correlation algorithm and to ensure that the performance of a photon-PCL with signal and noise level was correctly treated. Figure 6a shows a simulation of a traditional full-waveform signal with a Gaussian laser pulse. The Gaussian pulse can be replaced by a chirped pulse as shown in Figure 6b. Applying that to a simulated waveform results in the return waveform shown in Figure 6c. This is the return that would be measured by a full-waveform detector with no noise. To convert this to a photon-PCL signal, that noise-free full-waveform simulation is taken as the probability distribution function for returned photon ranges (i.e., there is a higher probability of getting a return from an elevation with higher intensity) and the number of photons selected from it. The total number of photons per laser shot is selected from a Poisson distribution with the mean specified by Equation (10), converted to number of photons. Within the simulator, the noise rate (dark count plus background light) is defined in terms of noise photons per microsecond, and that number of photons (again selected from a Poisson distribution about that mean) is scaled by the detection window size and added at random ranges. The resulting train of photons is binned to make a pseudo-waveform, as in Figure 6d (showing an example for 4000 photons), and shot noise is added by applying white Gaussian noise to each bin with a standard deviation equal to the square root of the number of photons in that bin.

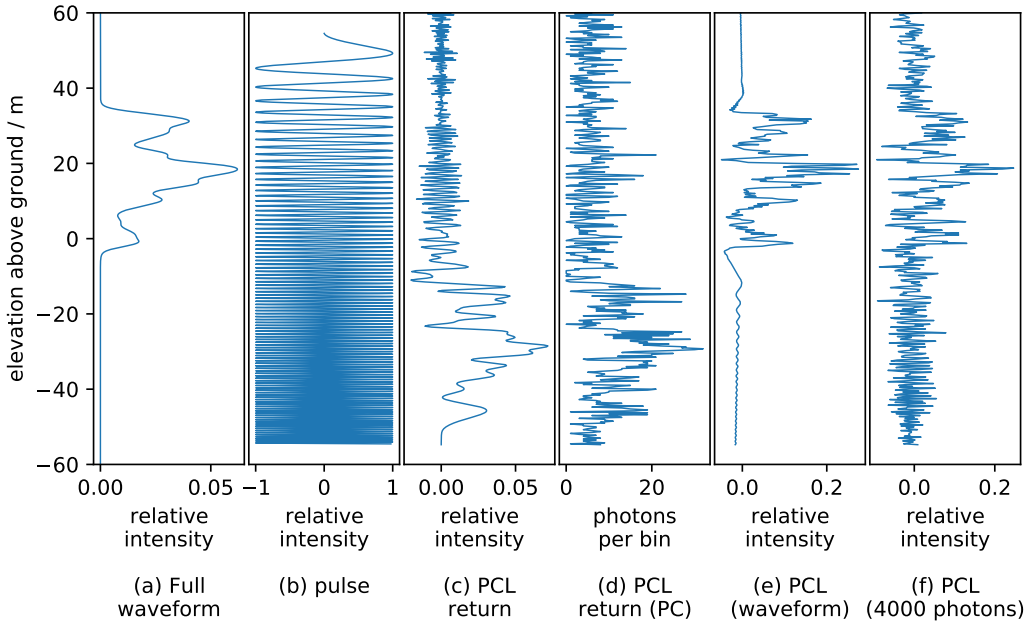

Figure 6. This figure demonstrates the convolution and cross-correlation steps in recovering the waveform using a Pulse Compressed Lidar (PCL): (**a**) shows the full waveform, i.e., the true point density we are trying to observe; (**b**) shows the emitted pulse, a linear chirp; (**c**) shows the convolution of (**a**) with (**b**) as this is what would be measured by a full-waveform detector applying PCL; (**e**) is the reconstruction of the original signal from the cross-correlation of (**c**) with the pulse shape (**b**); (**d**) shows the same return signal in (**c**), but measured with a photon couting rather than a full-waveform detector; and (**f**) shows the reconstructed signal from (**d**).

The pseudo-waveform in Figure 6d is what the photon-PCL lidar would measure for a single footprint. To extract measurements of the ground from this, it must be cross-correlated with the original pulse (Figure 6b). Then it can be treated like a traditional full-waveform signal, removing background noise and smoothing and identifying ground returns. Cross-correlating the full-waveform return (Figure 6c) with the pulse gives the retrieved waveform in Figure 6e, whereas cross-correlation with the photon counting returns results in the signal shown in Figure 6f. It can be seen that the waveform in Figure 6e is very similar to what would have been retrieved by a full-waveform lidar with

the energy emitted in a 15.6 ns long-pulse (necessitating an 8% efficient solid-state laser) in Figure 6a, except for cross-correlation artifacts (ringing) at the tails of the signal. Both of these should give similar ground elevation and canopy height estimates when decomposed into Gaussians and the lowest taken as the ground elevation as demonstrated in Figure 7. The photon counting result in Figure 6f exhibits a lot more noise-like artifacts due to the signal discretization, illustrating why a large number of return photons may be required for reliably distinguishing the ground signal from the background noise. The simulator code is available open-source from: https://bitbucket.org/StevenHancock/gedisimulator (accessed on 4 April 2022.)

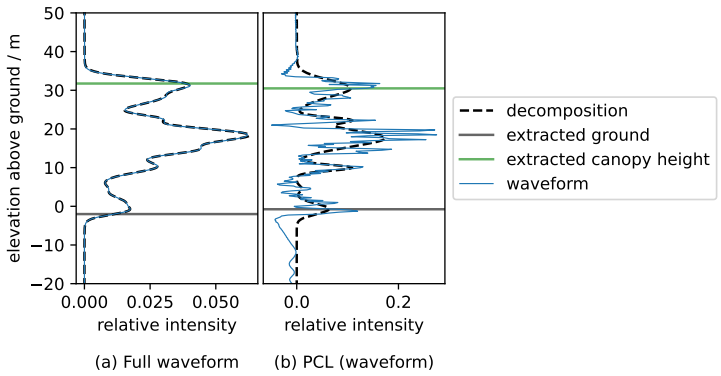

Figure 7. This figure demonstrates the ground extraction from Gaussian decomposition for (**a**) the full waveform case and (**b**) the waveform PCL case. The waveforms are shown in blue, the Gaussian decomposition as a dashed black line, the extracted ground as a solid gray line and the extracted canopy height as a solid green line. The ground and canopy height are computed as the mean of the lowest and highest Gaussian in the decomposition, respectively.

3.1.1. Simulator Validation

The primary function of the simulator is to determine the minimum signal strength needed for an accurate measurement from a spaceborne photon-PCL instrument. For the simulator predictions to be reliable, the simulated waveforms must show the same measurement accuracy as a function of signal strength and noise rate as observed in the real instrument. To determine whether the simulator was realistic enough to answer this question, we repeated the analysis in Hancock et al. [20] and performed a validation experiment comparing the simulated lidar signals against those measured by Fraunhofer CAP's bench instrument.

The bench instrument used a pulse chirp with a peak frequency of 125 MHz spread over a 60 m sweep. This was reflected from a hard target, and the returned signal was recorded by a photon-counting detector. Repeat measurements were made and combined to allow large photon counts while avoiding detector dead time or first photon bias. The total number of signal photons and the average background photon rate (from background light and electronic noise) were recorded. In the experiment, signal and background photon rates were controlled by laser voltage and exposure time, where a higher laser voltage yields a higher signal photon number and a longer exposure time increases both signal and background photon rates. The noise photon rate in this case only depended on exposure time and was 20, 130 and 200 total photons for exposure times of 5 µs, 50 µs and 100 µs, respectively. Higher effective noise rates resulted in cases where the signal was taken as a mean of repeated individual measurements.

Based on the pulse shape as well as signal and noise photon rates, repeated simulations were performed to replicate the experimental setup. Both the experimentally measured and simulated retrieved lidar signals were passed through the same signal-processing algorithm (cross-correlation), and the resulting SNR was calculated from both.

3.1.2. Signal Processing

The ground-finding algorithm in the lidar simulator relies on a series of signal processing steps to reduce the noise. The nature and scale of these denoising filters can be controlled by several tuning parameters:

`varScale` controls the signal detection threshold as a number of standard deviations above background [50];

`minWidth` controls the minimum number of consecutive bins that must lie above the threshold [50];

`sWidth` sets the smoothing width in meters;

`hann` applies a Hann filter with the specified number of bins [51].

Additional parameters exist for the PCL case, where smoothing can be applied before or after the cross-correlation step. The optimum set of denoising steps depends on the signal-to-noise ratio and will in general be optimized independently for different conditions on the ground.

For the results presented in this paper, all simulations were performed over a grid of these tuning parameters. The explored parameter space consists of `sWidth` from 0 to 1 (in meters), `varScale` from 1.5 to 7 (in standard deviations) and `hann` from 1 to 17 (in number of bins). The `minWidth` parameter was largely superseded by the Hann filter. All results presented in this paper reflect the optimum found across this parameter grid.

3.2. ALS Datasets

For calibration of the minimum detectable energy, the simulator was run over six ALS datasets with a variety of canopy cover, canopy height, and ground slope distributions. The datasets and their properties are summarized in Table 3.

Table 3. This table gives a summary of the canopy and ground properties for the ALS datasets used for the simulations. Each property is given as mean ± standard deviation.

Site	Biome	Canopy Cover (%)	Ground Elevation (m)	Ground Slope (Degree)	Canopy Height (m)	Reference
Sonoma	Mediterranean Forests, Woodlands and Scrub	65 ± 30	208 ± 80	18 ± 11	25 ± 14	[52]
La Selva	Tropical and Subtropical Moist Broadleaf Forests	68 ± 36	77 ± 35	10.0 ± 9.1	22 ± 12	[53]
Bartlett	Temperate Broadleaf and Mixed Forests	84 ± 20	510 ± 170	16.1 ± 9.4	19.3 ± 5.2	[54]
Wind River	Temperate Conifer Forests	75 ± 18	680 ± 240	18 ± 12	32 ± 12	[54]
Robson Creek	Tropical and Subtropical Grasslands, Savannas and Shrublands	97.7 ± 3.5	860 ± 140	22 ± 10	32.7 ± 5.6	[55]
Oak Ridge	Temperate Broadleaf and Mixed Forests	63 ± 39	272 ± 31	9.3 ± 7.7	19 ± 11	[54]

From each dataset, a stratified sample of 2000 footprints was randomly selected across 100 canopy cover strata, with an equal number of samples in each 1% bin. Even though the canopy cover distributions of all sites were non-uniform, sufficient footprints in each strata were available for all sites except for Robson Creek. Due to the high forest density at this site, very few footprints exhibit a canopy cover of less than 80%.

Figure 8 shows five simulated sample waveforms at different canopy covers, with the true ground marked as a dashed line. This illustrates how the ground signal is generally decreasing with increasing canopy cover. The true ground is obtained from the center of gravity of the ALS ground points and may therefore carry a small error in itself if ground points are misclassified.

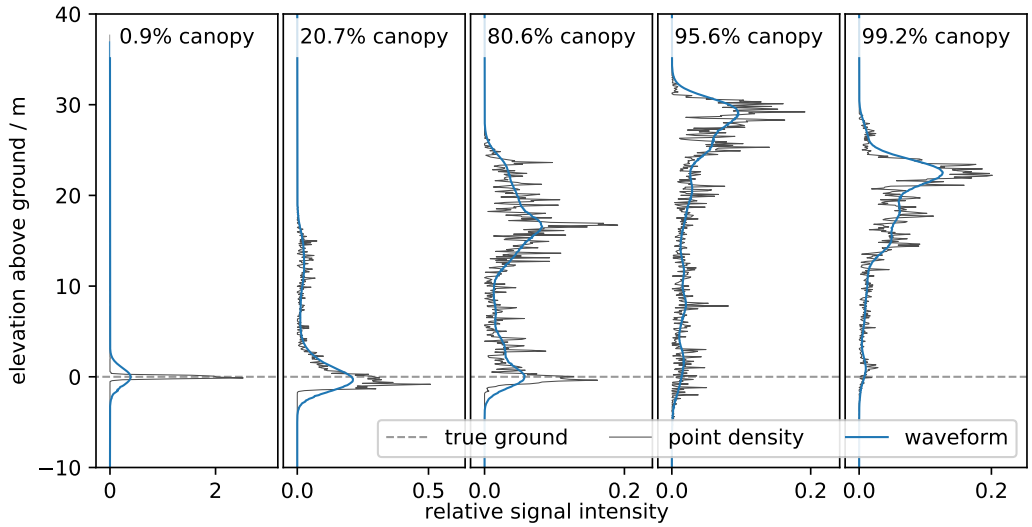

Figure 8. This figure shows five examples of simulated waveforms for different canopy cover percentages. The ALS point density is shown in gray, the simulated waveform in blue, and the true ground as a dashed line. The relative intensity of the measured ground signal decreases with higher canopy cover as fewer signal photons pass through the canopy to be reflected off the ground.

3.3. Beam Sensitivity Calculation

The beam sensitivity is defined as the canopy cover limit at which the ground can still be reliably detected. It is therefore a dimensionless quantity between 0 and 1. There are two ways to estimate the beam sensitivity in our simulations. The first approach is to estimate it theoretically from the signal-to-noise ratio of the ground return. In an alternative approach, we can estimate it empirically from a graph of the ground error distribution against canopy cover percentage.

3.3.1. Estimation from Signal-to-Noise Ratio

The signal-to-noise ratio (SNR) of a waveform lidar can be expressed as the beam sensitivity, which gives the canopy cover at which a ground return will have a 90% chance of being detectable above the background noise. This can be calculated analytically from a noised waveform from the integral of the signal return and the statistics of the background noise (whether background light, electronic noise or signal processing artifacts) [20].

To analytically calculate it, first a noise threshold must be set to give a certain probability of avoiding a false positive from noise (set as 95% in this case). Then the amplitude that a single return must extend above to give less than a certain probability of a false negative (set as 10% here) is calculated. The width of that return is used with the amplitude to find the integral of that single return. The ratio of this single return integral to the integral of the total signal gives the minimum fraction of total return energy that can be contained within a single feature (such as the ground return) and detected with that probability of a false positive and negative.

To calculate this, we need the distribution of the noise intensity after any smoothing and minimum widths have been applied. The noise threshold is then set at the 95% point on the cumulative integral of the noise distribution. Next, the amplitude of a ground return above that is needed. This amplitude difference is set as the 10% point on the cumulative integral of the noise distribution. The amplitude of the single return, A_s, is then equal to the sum of these two values.

Finally, the width of the single return is needed to calculate the integral (see Figure 2). The width of the ground return is controlled by the ground slope, the width of the lidar's sys-

tem pulse and any smoothing that has been applied to the signal. From Hancock et al. [20] (Equation (7)), the ground return's effective width σ_{eff} is given by:

$$\sigma_{\text{eff}} = \sqrt{\sigma_p^2 + \sigma_s^2 + \sigma_f^2 \tan^2 \theta} \tag{11}$$

where σ_p is the system pulse width, σ_s is the smoothing width applied, σ_f is the footprint width, and θ is the ground slope. For a single pulse or a pulse train lidar, σ_p is equal to the standard deviation of the pulse shape (a single repetition for a pulse train). For a PCL lidar, σ_p is the width that would result from a perfectly noise-free cross-correlation with the convolution of pulse with a Dirac delta. For a cross-correlated chirped pulse, pulse width, σ_p, is theoretically controlled by the frequency bandwidth within the chirped pulse by:

$$\sigma_p = \frac{c}{\Delta f_{\text{chirp}}} \tag{12}$$

where c is the speed of light, and Δf_{chirp} is the difference between the pulse's peak and minimum frequency (can be approximated as equal to the peak frequency).

Once the width of the ground return is defined by Equation (11), the integral, I_s, can be found assuming a Gaussian return (which a lidar return is likely to be close to, after cross-correlation or smoothing).

$$I_s = \sigma_{\text{eff}} A_s \sqrt{2\pi} \tag{13}$$

The beam sensitivity, b_s, is then:

$$b_s = 1 - \frac{I_s \frac{\rho_v}{\rho_g}}{I_0} \tag{14}$$

where I_0 is the integral of the waveform above mean noise level, and ρ_v/ρ_g is the ratio of the canopy and ground reflectance. I_0 can be calculated for a range of smoothing widths and minimum feature widths to select the optimum parameter configuration. For photon-counting detectors, only discrete whole numbers of photons can be detected. To prevent non-physical decimal numbers of photons being used to estimate a beam sensitivity, the beam sensitivity is truncated to zero if there is less than a 90% probability of detecting at least one ground photon.

3.3.2. Estimation from Ground Error Distribution

As a sanity check, we can extract the beam sensitivity empirically from simulation data by fitting a curve to a scatter plot of the ground error vs. canopy cover. The beam sensitivity can then be calculated from the fit parameters and a ground error threshold. An example is shown in Figure 9, where a curve with the equation $f(x) = a + e^{b(x-c)}$ is fitted. The error threshold for the ground detection is determined by calibrating the extracted beam sensitivity against benchmark simulations with known beam sensitivity, as detailed in Appendix B.

In general, the results from this method are considered an empirical validation of the results obtained from the SNR, and it is the latter that forms the basis for our quantitative comparative analysis.

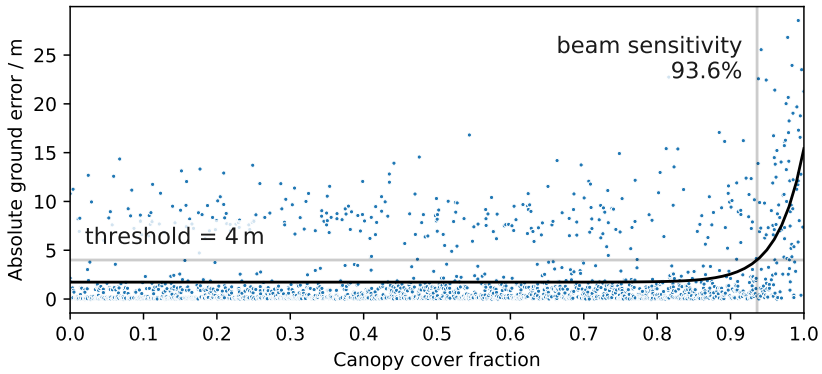

Figure 9. This figure demonstrates the beam sensitivity extraction for a PCL scenario with 5000 photons. The blue markers represent returns from individual footprints, and the black line is the resulting curve fit. With the threshold set to 4 m, the extracted beam sensitivity is 93.6%.

3.4. Experiments

Using the lidar simulator, we ran a series of experiments to assess the possible combinations of laser source (Section 2.2) and laser modality (Section 2.3) in terms of their beam sensitivity and ultimately their energy and power requirements. While all of our simulations assume a photon-counting detector, we compare the final results to the true parameters of the GEDI mission as a representation of a solid-state laser with full-waveform detector. We assume a telescope diameter of 80 cm (area of $\approx$0.5 m^2) for all simulations. This corresponds to the telescope diameter for both ICESat-2 and GEDI (see Table 1).

Each of the cases outlined below was simulated for six samples of 2000 waveforms each corresponding to the six ALS datasets and for a range of signal photon numbers. The beam sensitivity was then calculated for each case and each photon number, resulting in a curve of beam sensitivity as a function of photon count. From these curves, we extracted the required number of photons to achieve the target beam sensitivity of 98% and calculated the corresponding energy and power requirements. Finally, we compared all scenarios based on these requirements.

3.4.1. Solid-State Lasers

Because solid-state lasers are not limited by their peak power, the only modality that we tested for this laser source is a conventional single pulse (Section 2.3.1) with no pulse repetition ($N_{\text{rep}} = 1$). The case of a full-waveform detector was taken from the literature values for GEDI's coverage beams [2]. For the photon-counting detector case, the detector integration time in this case is about 1 µs, which at a noise photon rate of 0.012 µs^{-1} gives a total expected number of noise photons of 0.012. As discussed in Section 2.4, the high signal photon rate requires the use of a photon detector array with a PDE of $Q = 0.31$.

As an additional check of the estimated powers derived from the simulator, the ground elevation errors in ICESat-2 data were analyzed as a function of the number of ground photons over Sonoma County. ICESat-2 photons were taken from the ATL03 Global Geolocated Photon Data product, version 4 [56], and any geolocation offsets relative to the ALS data were corrected using the PhoREAL package [57]. For each ICESat-2 footprint, an ICESat-2 waveform was simulated, divided into ground and canopy components, and used to reclassify ATL03 photons as ground, canopy or noise. Only ICESat-2 segments that had similar noise rates to the nighttime rates used here were analyzed (0 µs^{-1} to 0.024 µs^{-1}). The numbers of ground photons were scaled by a factor of 50 to give the total number of signal photons needed to detect the ground through 98% canopy cover, and the root mean square ground elevation error calculated against ALS data.

3.4.2. Diode Lasers

For the diode laser, we tested a pulse train modality (Section 2.3.2) and PCL (Section 2.3.3), each with a number of pulse repetitions of $N_{\text{rep}} = 4000$. This is the maximum number

of repetitions to allow for an unambiguous range of $r_{ua} = 150$ m within the 4 ms dwell time (considering the two-way distance). Because of the low signal photon rate with a low-power diode laser, these cases do not require a photon detector array, and the detector efficiency is $Q = 0.58$. The detector integration time for both modalities is 4 ms.

4. Results

4.1. Simulator Validation

As described in Section 3.1.1, the PCL mode of the lidar simulator was validated against empirical results from laboratory experiments. Figure 10 shows an example pulse-compressed waveform for three different signal photon rates, along with the corresponding results of the cross-correlation.

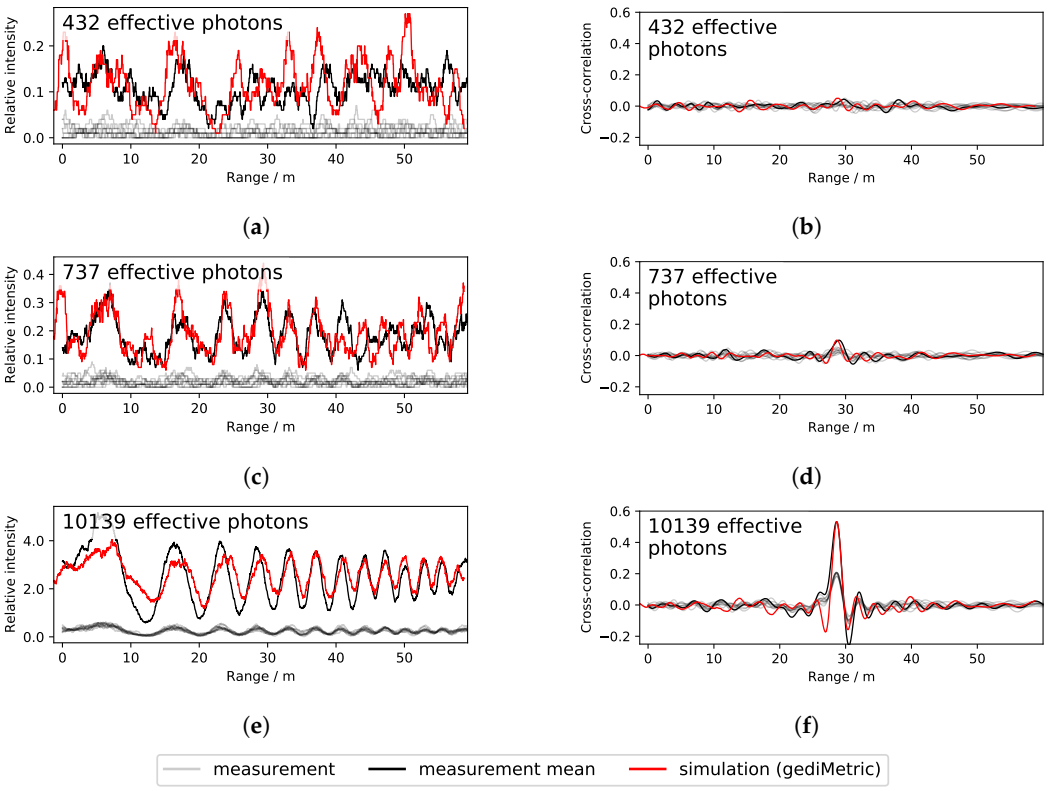

Figure 10. This figure shows the measured photon returns (**a**,**c**,**e**) and the corresponding cross-correlations (**b**,**d**,**f**) for the laboratory validation of the lidar simulator. Experimental results are shown in black, the simulated results in red. The faint gray lines represent the individual laboratory measurements, which were added up to yield the black curves: (**a**) PCL waveform return (432 photons); (**b**) Cross-correlation (432 photons); (**c**) PCL waveform return (737 photons); (**d**) Cross-correlation (737 photons); (**e**) PCL waveform return (10,139 photons); (**f**) Cross-correlation (10,139 photons).

A qualitative comparison of these examples shows good agreement between experiment and simulation, especially for high photon counts. Discrepancies at very low photon rates are to be expected as an artifact of the noisy signal. For a more quantitative validation, we calculated the SNR for each experimental measurement and corresponding simulation as the ratio between the peak intensity and the standard deviation of the background noise. Figure 11 compares the SNR distributions between experiment and simulation. Figure 11a shows the SNR as a function of number of photons, whereas Figure 11b shows a direct comparison of experimental and simulated SNR.

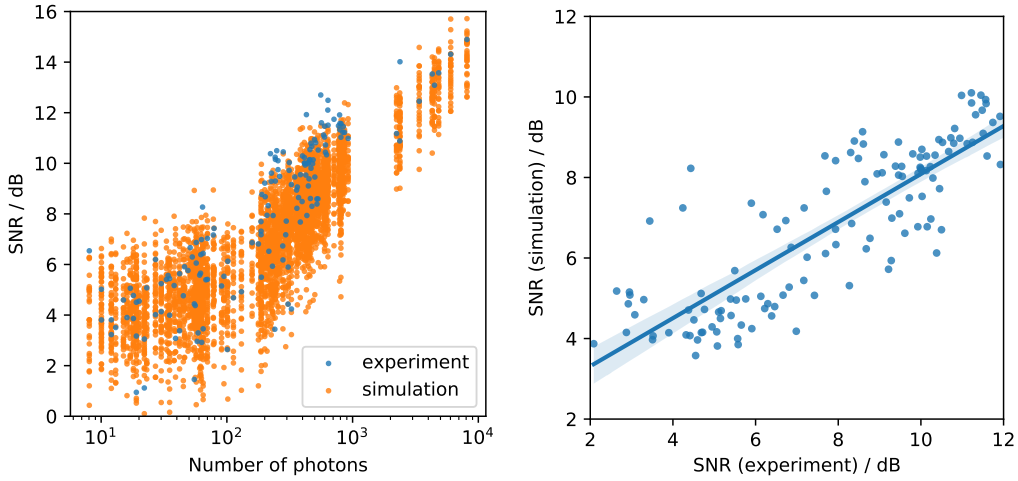

(**a**) (**b**)

Figure 11. SNR. This figure shows an analysis of the experimental and simulated SNR when measuring a single hard target using PCL: (**a**) shows the SNR distribution as a function of number of photons; and (**b**) shows a linear regression of simulated and experimental SNR, where each marker represents one number of photons. The correlation coefficient is 0.86. (**a**) SNR as a function of number of photons; (**b**) Simulated and experimental SNR.

From Figure 11b, the correlation coefficient was computed as 0.86, indicating a strong correlation between the experimental and simulated SNR. While there is a small disagreement between the SNR of simulation and experiment, a perfect correlation is prevented by the randomness inherent in photon counting. Given the validation study, we can now be confident that the simulator is able to assess the accuracy of a future spaceborne PCL system.

4.2. Solid-State Lasers

Solid-state lasers represent the default for current space-borne applications. As discussed in Section 2.2, they allow for a high power output and thus only require a single pulse to collect sufficient energy. This means the overall noise rate is low and the SNR high.

Photon Counting

Having calibrated the beam sensitivity extraction for the full-waveform Gaussian pulse case, we could calculate the beam sensitivity for photon counting as a function of the number of detected photons (Figure 12). A single pulse requires high peak power to pack sufficient energy into the short pulse duration and thus is only feasible with a solid-state laser. The short integration time also means that the number of noise photons is near zero.

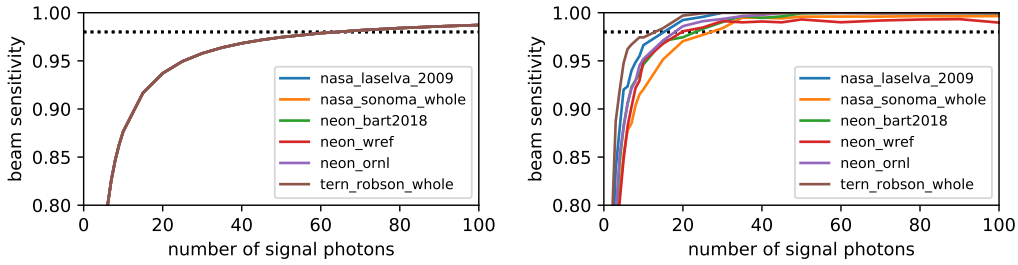

(**a**) (**b**)

Figure 12. This figure shows the beam sensitivity as a function of the number of signal photons for a solid-state laser operating with a single pulse and an accordingly low noise rate. Around 60 photons are required to reach 98% beam sensitivity. (**a**) Computed from signal-to-noise ratio; (**b**) Empirically estimated from ground error.

For low photon numbers, the beam sensitivity computed from the SNR accounts for quantization effects by requiring a probability of at least 90% of encountering one whole ground photon (see Section 3.3.1). In this case, the SNR method predicts a beam sensitivity of 98% from around 60 photons. The estimate from the ground error (Figure 12b) predicts that only 20 photons are required to achieve 98% beam sensitivity. At such low photon numbers, however, noise near the true ground may be mistakenly classified as ground, making the ground error estimate unreliable. This was confirmed by the analysis of real ICESat-2 data, which also showed that ground elevation RMSE dropped to sub-3 m for 60 or more signal photons per laser shot.

From theoretical considerations, at 98% canopy cover and zero noise at least 50 photons should be necessary to receive one ground photon, on average. In general, the ground error estimates are treated as a sanity check and validation of the SNR results which provide a more theoretical beam sensitivity estimate.

At a wavelength of $\lambda = 850\,\text{nm}$, 60 photons correspond to a detected energy of $E_{\text{det}} = 0.014\,\text{fJ}$.

4.3. Diode Lasers

4.3.1. Pulse Train

One alternative laser modality is the pulse train approach. For the sake of the simulations, a pulse train may be treated the same way as a single pulse, except that the same energy (i.e., number of signal photons) is collected over a longer integration time through pulse repetition, also causing an accumulation of noise photons.

As for the solid-state case, Figure 13 shows the beam sensitivity as a function of signal photon number for all six sites. The number of noise photons depends on the integration time (i.e., number of repeats), the bandpass filter width, the detector efficiency, and the laser energy, as described in Section 2.5.

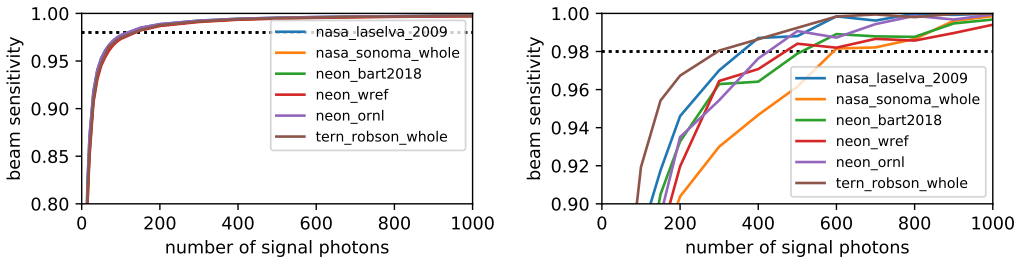

Figure 13. This figure shows the beam sensitivity as a function of the number of signal photons for a diode laser pulse train with 4000 repetitions. Because of the larger number of noise photons compared to the solid-state laser, around 115 photons are required to reach 98% beam sensitivity. (**a**) Computed from signal-to-noise ratio; (**b**) Empirically estimated from ground error.

While in principle very similar to the single-pulse approach, in the case of a solid-state laser, the much larger number of detected noise photons means that a significantly higher number of signal photons is required for the ground to be detectable at the low SNR. The sensitivity curves computed from the SNR (Figure 13a) show that 115 photons are required to achieve 98% beam sensitivity with the pulse train approach. This corresponds to a detected energy of 0.027 fJ. The sensitivity curves from the ground error distribution (Figure 13b) exhibit a similar shape and order of magnitude of the photons required but differ in their absolute values and show more variation across sites. This is expected as the ground error estimation depends both on the quality of the assumed true ground and the performance of the ground detection algorithm.

4.3.2. PCL

All results presented in this section are for PCL with frequency chirps as introduced in Section 2.3.3. While we have tested other pulse shapes, including maximum length sequence (MLS) and Zadoff-Chu sequences, we have found no improvement over the frequency chirp. In particular, we used a chirp with a sweep distance of 100 m (333 ns) and a start frequency of 1 MHz. We then investigated the effect of varying the stop frequency between 100 MHz and 2 GHz.

Figure 14 shows the beam sensitivity curves for PCL with frequency chirps. Eight different peak frequencies were tested, ranging from 100 MHz to 2 GHz, and are represented in the figure as different shades of purple (darker shades represent higher peak frequencies). The data shown is for the La Selva site (Table 3).

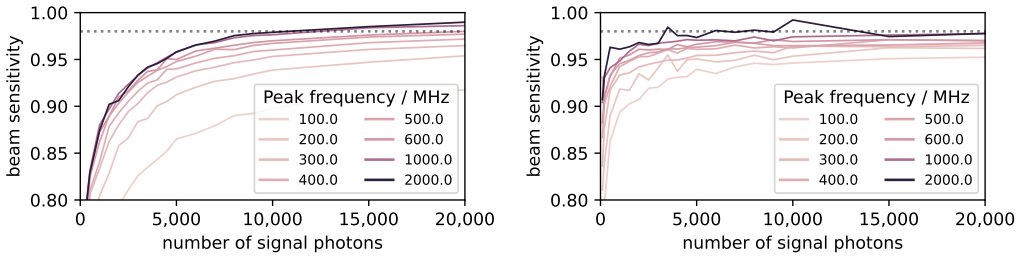

Figure 14. This figure shows the beam sensitivity as a function of the number of signal photons for a diode laser in PCL mode with frequency chirps, for a range of peak frequencies. There are 4000 pulse repetitions. (**a**) Computed from signal-to-noise ratio; (**b**) Empirically estimated from ground error.

There is a clear increase in beam sensitivity for higher frequencies, although the increase is starting to become marginal at 1 GHz. Frequencies higher than 2 GHz have not been tested, both because of diminishing returns and because such frequencies are stretching the engineering limits for laser modulation.

Figure 15 shows the beam sensitivity curves for all six sites at 2 GHz.

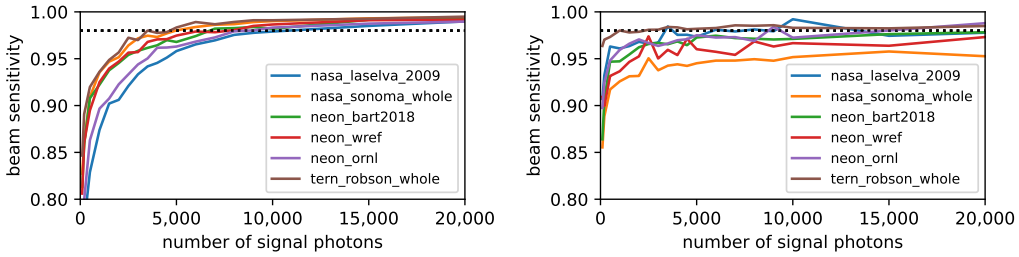

Figure 15. This figure shows the beam sensitivity as a function of the number of signal photons for a diode laser in PCL mode with 2 GHz frequency chirps for all sites. In this case, more than 10,000 photons are required to reach 98% beam sensitivity. (**a**) Computed from signal-to-noise ratio; (**b**) Empirically estimated from ground error.

At Sonoma and Wind River, the comparatively large tree heights (see Table 3) increase the possible magnitude of ground errors as compared to sites with smaller tree heights, leading to lower sensitivites when estimated from the ground error (Figure 15b). While the ground error estimates plateau at a lower maximum beam sensitivity, they support the conclusions that about 10,000 photons are required to reach the target sensitivity of 98%. For the La Selva site, the number of photons is 11,400, corresponding to a detected energy of 2.66 fJ.

4.4. Comparison of E_{det} Values

The results for the solid-state laser, diode laser with pulse train and diode laser with PCL from the previous sections are summarized for a direct comparison in Table 4. In addition, the table contains a full waveform column for the solid-state laser, which corresponds to the GEDI configuration, except the system parameters such as payload power, altitude and telescope area have been matched to the three photon counting scenarios. GEDI has been designed to have 98% beam sensitivity and so serves as a benchmark.

Table 4. This table compares the different laser modalities in terms of their expected signal and noise photon counts as well as the required average and peak laser output power.

	Source	**Solid-State**		**Diode**	
	Modality	**Single Pulse**		**Pulse Train**	**PCL**
	Detector	**Full Waveform**	**Photon Counting**	**Photon Counting**	**Photon Counting**
scenario conditions	Q	0.58	0.31	0.58	
	L_e	0.11		0.25	
	N_{rep}	1		4000	
	$\Delta\lambda$	0.7 nm	30 pm	1 nm	
	T	≈1 µs	≈1 µs	4 ms	
at 98% sensitivity	N_{photons}	1500 [a]	60	115	11,400
	N_{noise}	n/a	0.02	5.3	8.4
	E_{det}	0.28 fJ	0.014 fJ	0.027 fJ	2.66 fJ
	E_{shot}	2.6 mJ [b]	0.25 mJ	0.25 mJ	25.2 mJ
	P_{peak}	79.7 kW [b]	7.5 kW	1.9 W	14.9 W
	P_{avg}	0.66 W [b]	0.06 W	0.06 W	6.3 W
	swath	553 m	5898 m	13,085 m	132 m
	N_{sat}	4	1	1	15

[a] This number is calculated from the known E_{det} and wavelength of GEDI. [b] The actual values on GEDI are slightly higher at $E_{\text{shot}} = 5$ mJ, $P_{\text{peak}} = 160$ kW and $P_{\text{avg}} = 1.2$ W due to optical inefficiencies.

In this comparison, the solid-state photon counting setup still has the lowest required E_{det} by some margin (0.014 fJ). However, when considering the laser efficiency L_{e} and the detector efficiency Q, the diode laser in pulse train mode now gives the widest coverage with a swath width of 13,085 m compared to a solid-state laser that can achieve a swath width of 5898 m in photon counting mode and 553 m in full waveform mode (GEDI). It therefore requires only one satellite for global coverage within 5 years, the same number as for a solid-state laser with a photon-counting detector, and less than the four satellites required in full waveform mode. Because the PCL mode requires significantly higher numbers of signal photons to achieve the same beam sensitivity, it has the highest required detectable energy and the lowest swath width and is therefore the worst contender by this metric. The diode laser also has a lower required power than the the solid-state laser. However, the maximum possible output power is also the main limitation for this type of laser.

5. Discussion

We have assessed three configurations of a space-borne lidar instrument in detail: (1) a solid-state laser operating in a single-pulse mode with photon-counting detector, (2) a diode laser operating in a pulse train mode with photon-counting detector, and (3) a diode laser in PCL mode, also with photon counting detector.

The goal here was to investigate the feasibility of a diode laser for applications in space-borne lidar instruments because of its up to five times higher laser efficiency. We have found that the minimum detectable energy E_{det} necessary for ground detection at up to 98% canopy cover is 0.014 fJ for the solid-state laser, 0.027 fJ for the diode laser with pulse train and 2.66 fJ for the diode laser with PCL. When taking into account the laser efficiency L_{e} and the detector efficiency Q, we can compare the number of satellites required for global coverage within five years between the configurations, and we end up with a single satellite for the solid-state laser and for the diode laser with pulse train and 15 satellites for the diode laser with PCL.

The diode laser in pulse train mode achieves the greatest overall coverage due to the higher laser efficiency and can provide two times larger coverage compared to a solid-state laser at effectively the same mission cost (13,085 m compared to 5898 m swath width for a single satellite).

Another consideration is the overall power requirement. This is the main limitation of the tapered diode lasers as they can typically only operate at powers between 5 and 8 W [31]. The pulse train approach has the lowest peak power requirement at 1.9 W, followed by 14.9 W for PCL and compared to 7.5 kW and 79.7 kW for the solid-state laser in photon counting and full waveform mode, respectively. While the peak power for the pulse train is well within the current technological capability, the power required for the PCL mode remains beyond what is currently feasible with tapered diode laser technology.

The results for the diode laser are based on a 25% laser efficiency as derived in Section 2.2, which takes into account the electrical-to-optical efficiency of the diode laser itself and the efficiency of the thermo-electric cooler used to extract waste heat from the laser. However, the overall efficiency may be lower depending on the efficiency of the driver electronics providing the electrical power to the laser itself due to the challenges of switching multi-amp currents on nanosecond timescales. This will require attention in future phases of development to realize the potential of diode lasers for this application. Thermal management solutions will also need to be tailored for satellite compatibility, but this is not expected to impact efficiency significantly.

Our estimates are based on the assumption that we can in fact operate a diode laser at the required peak powers. Coherent Inc., one of the major manufacturers of tapered amplifiers, has reported peak powers of 25 W for 50 µs duration pulses at 976 nm with 50% duty cycle [31] (slide 17), and it is possible that even higher peak powers could be achieved with shorter pulse durations such as the ∼30 ns pulses required for the present application [33]. This makes the pulse train approach a feasible modality with its peak power requirement of 1.9 W. Therefore, a diode-laser-based satellite lidar system may soon be realizable with currently available diode laser technology.

It is important to note that this study has focused entirely on energy/power considerations. The swath width achieved in practice may be limited by other factors such as the number of lasers and detectors that can be deployed on a practical satellite platform. Future phases of the work will examine these system-level trade-offs in detail to identify the most cost-effective approach. Such challenges affect both solid-state- and diode-laser-based systems, with diode lasers taking up less volume and contributing less mass, while solid-state lasers, with their high pulse energies may provide multiple ground tracks from a single beam that is split. The balance of these benefits and constraints, along with the capabilities of different satellite platforms and associated launch costs, will determine the optimal solution.

6. Conclusions

This paper was motivated by the need to improve spaceborne lidar coverage and by the notable absence of diode lasers in spaceborne lidar instruments. Solid-state lasers are currently the preferred choice due to their ability to operate at high powers, a necessity for emitting high-powered pulses as required for receiving sufficient return energy when emitting from space. While diode lasers cannot currently emit sufficient energy in a single pulse, their higher laser efficiency, as well as smaller size and mass, makes them a promising candidate for use in space, where the available power is a constraint. We have assessed potential modes of operation for a diode laser that would result in the same ground-finding accuracy as a solid-state laser. In particular, our target was set at a beam sensitivity of 98%, i.e., we require a 90% chance of detecting the ground through 98% canopy cover. With currently demonstrated technology, the achievable swath width is 553 m for a solid-state laser with full-waveform detector (such as GEDI), 5898 m for a solid-state laser with photon-counting detector (a higher energy ICESat-2), 13,085 m for a diode laser in pulse train mode

and 132 m for a diode laser in PCL mode. These swath width estimates are based on the total number of lasers that could be supported by a payload power of 240 W.

From these results, we can formulate the following main conclusions:

(a) A solid-state laser with photon-counting detector still requires the lowest detectable energy overall.
(b) Based on energy and power requirements alone, a diode laser with a pulse train configuration can provide a two times wider coverage than a solid-state laser with a swath width of 13,085 m, while at the same time requiring less than 0.1% of the peak power.
(c) Compared to a pulse train, PCL requires significantly larger photon numbers to achieve the same beam sensitivity due to the cross-correlation artifacts introduced by a discrete photon counting return signal. It is therefore probably not the optimum configuration for a diode laser lidar.
(d) The anticipated system cost for global coverage in 5 years can potentially be reduced when using a diode laser compared to a solid-state laser, as the same coverage may be achieved with a smaller satellite.

The achievable swath width for the diode laser is so much higher than for the solid-state laser because of the combined benefits of a two times higher laser efficiency and a two times higher detector efficiency, despite a requirement to detect 115 rather than 60 photons. As discussed, the actual swath width in a practical system may be subject to additional constraints that are independent of the type of laser source.

Future work to improve the signal processing for Pulse Compressed Lidar on photon-counting detectors may result in the reduction of cross-correlation artifacts through optimizing the pulse shape and noise suppression algorithms, which in turn would reduce the energy requirements for this modality. Meanwhile, the power requirement for a diode laser in pulse train is low enough to be achievable with presently available technology.

In conclusion, considering the technological advancements in diode laser power and laser and detector efficiency, diode lasers are becoming a feasible option in spaceborne instruments. The smaller size and mass of diode lasers makes them a promising choice for future satellites, and we see a clear opportunity for diode-laser-based satellite lidars.

Author Contributions: Conceptualization, S.H. and L.P.; methodology, S.H.; software, S.H. and J.N.H.; validation, J.N.H., H.C., S.H. and M.P.; formal analysis, J.N.H.; writing—original draft preparation, J.N.H. and S.H.; writing—review and editing, J.N.H., G.M.B., B.E.J., S.H. and I.D.; visualization, J.N.H.; supervision, S.H.; funding acquisition, S.H. All authors have read and agreed to the published version of the manuscript.

Funding: This research was funded by UKSA grant number NSIP20_N08.

Data Availability Statement: This research has made use of publicly available ALS datasets provided by the National Ecological Observatory Network (NEON), the UMD-NASA Carbon Mapping/Sonoma County Vegetation Mapping and LiDAR Program, the Northrop Grumman Corporation, and the AusCover Facility of the Terrestrial Ecosystem Research Network (TERN). The datasets are available at https://doi.org/10.5069/G9G73BM1 (Sonoma County), https://doi.org/10.5069/G9P8491K (La Selva), https://doi.org/10.48443/917D-G459 (Wind River, Bartlett, and Oak Ridge), and ftp://qld.auscover.org.au/airborne_validation/lidar/robsons_creek/ (Robson Creek) (accessed on 4 April 2022).

Acknowledgments: We would like to thank James Morris for starting the conversation that led to this project. We also want to thank Tom Neumann, Amy Neuenschwander, and Anthony Martino for their help in understanding the ICESat-2 noise rate.

Conflicts of Interest: The authors declare no conflict of interest. The funders had no role in the design of the study; in the collection, analyses, or interpretation of data; in the writing of the manuscript, or in the decision to publish the results.

Abbreviations

The following abbreviations are used in this manuscript:

ADC	analog-to-digital converter
ALS	Airborne Laser Scanning
CW	Continuous Wave
FWHM	full-width half maximum
MLS	maximum length sequence
PCL	Pulse Compressed Lidar
PDE	photon detection efficiency
SiPM	silicon photomultiplier
SNR	signal-to-noise ratio
SPAD	single photon avalanche diode
TEC	thermo-electric cooling
TRL	technology readiness level

Appendix A. Calculating Average and Peak Power

As E_{shot} must be emitted within the dwell time T_{dwell}, we can calculate the average power P_{avg} as

$$P_{\text{avg}} = \frac{1}{T_{\text{dwell}}} \int_{t=0}^{T_{\text{dwell}}} P(t)dt = \frac{E_{\text{shot}}}{T_{\text{dwell}}} \tag{A1}$$

The relationship between the average power and the peak power depends on the pulse shape and the number of pulse repetitions. For Gaussian pulses, it is related to the pulse width as measured by the standard deviation σ_{pulse} or the FWHM. These are linked by FWHM $= 2\sqrt{2\log 2}\sigma_{\text{pulse}}$. Therefore, for a pulse with FWHM $= 15.6$ ns, $\sigma_{\text{pulse}} \approx 6.6$ ns.

$$\int_{t=0}^{T_{\text{dwell}}} P(t)dt = \sqrt{2\pi} N_{\text{rep}} \sigma_{\text{pulse}} P_{\text{peak}} \tag{A2}$$

For chirps, the pulse is more spread out, resulting in a lower peak power for the same average power.

$$\int_{t=0}^{T_{\text{dwell}}} P(t)dt \approx 0.63 N_{\text{rep}} T_{\text{sweep}} P_{\text{peak}} \tag{A3}$$

where T_{sweep} is the chirp sweep duration (for a 100 m chirp, $T_{\text{sweep}} \approx 333$ ns).

The ratio of average and peak power is therefore

$$P_{\text{avg}}/P_{\text{peak}} \approx \frac{N_{\text{rep}}}{T_{\text{dwell}}} \times \begin{cases} 2.51\sigma_{\text{pulse}} & \text{for Gaussian pulses} \\ 0.63 T_{\text{sweep}} & \text{for a chirp.} \end{cases} \tag{A4}$$

Appendix B. Beam Sensitivity Benchmark

The beam sensitivity can be extracted empirically from simulation data by fitting an exponential curve of the form

$$y = a + e^{b(x-c)} \tag{A5}$$

to a scatter plot of the ground error vs. canopy cover. This function was chosen as it can adequately model a relatively constant error followed by a steep increase at higher canopy covers. The beam sensitivity can then be calculated from the fit parameters a, b, and c by setting a ground error threshold y_{thresh}:

$$b_s = c + \frac{1}{b} \log(y_{\text{thresh}} - a) \tag{A6}$$

The error threshold for the ground detection is determined by calibrating the extracted beam sensitivity against benchmark simulations with known beam sensitivity, ranging from 70% to 99%.

Figure A1 shows the resulting curves of empirically extracted vs. simulated (benchmark) beam sensitivity for different thresholds (between 2 and 7 m).

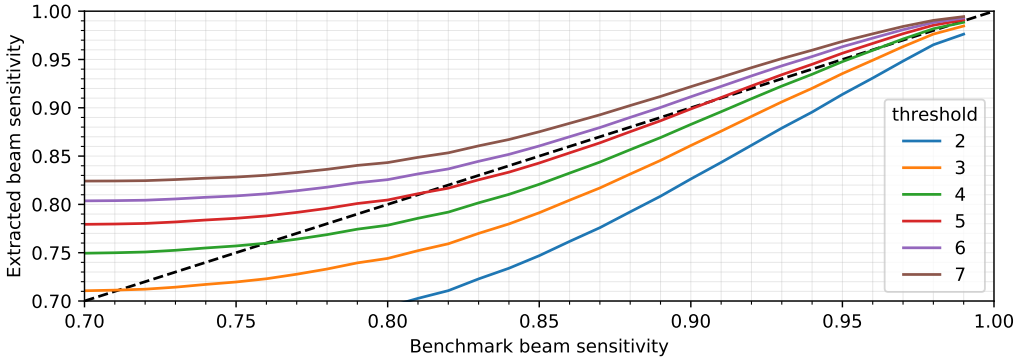

Figure A1. This figure shows the extracted beam sensitivity for a series of benchmark datasets with known sensitivity, for different error thresholds. The black dashed identity line is the target to reach.

While a threshold of 5 m gives results closest to the benchmark for the largest range of sensitivities, a 4 m threshold is certain to underestimate the beam sensitivity for values above 80% and is closest to the benchmark above 95%. We therefore use a 4 m threshold. The extracted beam sensitivity appears to reach a plateau for benchmark sensitivities below approximately 80%. This is not a concern, however, as our target sensitivity is above 90%.

For the beam sensitivity estimates using this method to be reliable, the canopy cover distribution must be near-uniform as a skewed distribution may introduce a bias in the curve fit (which was calibrated with respect to a uniform distribution). While none of the sites have a uniform distribution of canopy covers in the available footprints, the stratified sampling described in Section 3.2 allowed for uniform sampling distributions in all sites except for Robson Creek. The beam sensitivities cited for Robson Creek using this method may therefore show a positive bias and should not be relied upon.

References

1. Sun, G.; Ranson, K.; Kimes, D.; Blair, J.; Kovacs, K. Forest vertical structure from GLAS: An evaluation using LVIS and SRTM data. *Remote Sens. Environ.* **2008**, *112*, 107–117. [CrossRef]
2. Dubayah, R.; Blair, J.B.; Goetz, S.; Fatoyinbo, L.; Hansen, M.; Healey, S.; Hofton, M.; Hurtt, G.; Kellner, J.; Luthcke, S.; et al. The Global Ecosystem Dynamics Investigation: High-resolution laser ranging of the Earth's forests and topography. *Sci. Remote Sens.* **2020**, *1*, 100002. [CrossRef]
3. Markus, T.; Neumann, T.; Martino, A.; Abdalati, W.; Brunt, K.; Csatho, B.; Farrell, S.; Fricker, H.; Gardner, A.; Harding, D.; et al. The Ice, Cloud, and land Elevation Satellite-2 (ICESat-2): Science requirements, concept, and implementation. *Remote Sens. Environ.* **2017**, *190*, 260–273. [CrossRef]
4. Duncanson, L.; Neuenschwander, A.; Hancock, S.; Thomas, N.; Fatoyinbo, T.; Simard, M.; Silva, C.A.; Armston, J.; Luthcke, S.B.; Hofton, M.; et al. Biomass estimation from simulated GEDI, ICESat-2 and NISAR across environmental gradients in Sonoma County, California. *Remote Sens. Environ.* **2020**, *242*, 111779. [CrossRef]
5. Schneider, F.D.; Ferraz, A.; Hancock, S.; Duncanson, L.I.; Dubayah, R.O.; Pavlick, R.P.; Schimel, D.S. Towards mapping the diversity of canopy structure from space with GEDI. *Environ. Res. Lett.* **2020**, *15*, 115006. [CrossRef]
6. Patterson, P.L.; Healey, S.P.; Ståhl, G.; Saarela, S.; Holm, S.; Andersen, H.E.; Dubayah, R.O.; Duncanson, L.; Hancock, S.; Armston, J.; et al. Statistical properties of hybrid estimators proposed for GEDI—NASA's global ecosystem dynamics investigation. *Environ. Res. Lett.* **2019**, *14*, 065007. [CrossRef]
7. Friedlingstein, P.; O'sullivan, M.; Jones, M.W.; Andrew, R.M.; Hauck, J.; Olsen, A.; Peters, G.P.; Peters, W.; Pongratz, J.; Sitch, S.; et al. Global carbon budget 2020. *Earth Syst. Sci. Data* **2020**, *12*, 3269–3340. [CrossRef]
8. Healey, S.P.; Yang, Z.; Gorelick, N.; Ilyushchenko, S. Highly local model calibration with a new GEDI LiDAR asset on Google Earth Engine reduces landsat forest height signal saturation. *Remote Sens.* **2020**, *12*, 2840. [CrossRef]
9. Mitchard, E.T.; Saatchi, S.S.; White, L.; Abernethy, K.; Jeffery, K.J.; Lewis, S.L.; Collins, M.; Lefsky, M.A.; Leal, M.E.; Woodhouse, I.H.; et al. Mapping tropical forest biomass with radar and spaceborne LiDAR in Lopé National Park, Gabon: Overcoming problems of high biomass and persistent cloud. *Biogeosciences* **2012**, *9*, 179–191. [CrossRef]

10. Qi, W.; Lee, S.K.; Hancock, S.; Luthcke, S.; Tang, H.; Armston, J.; Dubayah, R. Improved forest height estimation by fusion of simulated GEDI Lidar data and TanDEM-X InSAR data. *Remote Sens. Environ.* **2019**, *221*, 621–634. [CrossRef]
11. Silva, C.A.; Duncanson, L.; Hancock, S.; Neuenschwander, A.; Thomas, N.; Hofton, M.; Fatoyinbo, L.; Simard, M.; Marshak, C.Z.; Armston, J.; et al. Fusing simulated GEDI, ICESat-2 and NISAR data for regional aboveground biomass mapping. *Remote Sens. Environ.* **2021**, *253*, 112234. [CrossRef]
12. Saatchi, S.S.; Harris, N.L.; Brown, S.; Lefsky, M.; Mitchard, E.T.; Salas, W.; Zutta, B.R.; Buermann, W.; Lewis, S.L.; Hagen, S.; et al. Benchmark map of forest carbon stocks in tropical regions across three continents. *Proc. Natl. Acad. Sci. USA* **2011**, *108*, 9899–9904. [CrossRef]
13. Baccini, A.; Goetz, S.; Walker, W.; Laporte, N.; Sun, M.; Sulla-Menashe, D.; Hackler, J.; Beck, P.; Dubayah, R.; Friedl, M.; et al. Estimated carbon dioxide emissions from tropical deforestation improved by carbon-density maps. *Nat. Clim. Chang.* **2012**, *2*, 182–185. [CrossRef]
14. Avitabile, V.; Herold, M.; Heuvelink, G.B.; Lewis, S.L.; Phillips, O.L.; Asner, G.P.; Armston, J.; Ashton, P.S.; Banin, L.; Bayol, N.; et al. An integrated pan-tropical biomass map using multiple reference datasets. *Glob. Chang. Biol.* **2016**, *22*, 1406–1420. [CrossRef] [PubMed]
15. Hill, T.C.; Williams, M.; Bloom, A.A.; Mitchard, E.T.; Ryan, C.M. Are inventory based and remotely sensed above-ground biomass estimates consistent? *PLoS ONE* **2013**, *8*, e74170. [CrossRef] [PubMed]
16. Ploton, P.; Mortier, F.; Réjou-Méchain, M.; Barbier, N.; Picard, N.; Rossi, V.; Dormann, C.; Cornu, G.; Viennois, G.; Bayol, N.; et al. Spatial validation reveals poor predictive performance of large-scale ecological mapping models. *Nat. Commun.* **2020**, *11*, 1–11. [CrossRef]
17. Hancock, S.; Mcgrath, C.; Lowe, C.; Woodhouse, I. Requirements for a spaceborne lidar with wall-to-wall coverage: A Global Lidar System. *R. Soc. Open Sci.* **2021**, *8*, 1–17. [CrossRef]
18. Harding, D.J.; Carabajal, C.C. ICESat waveform measurements of within-footprint topographic relief and vegetation vertical structure. *Geophys. Res. Lett.* **2005**, *32*. [CrossRef]
19. Hancock, S.; Lewis, P.; Foster, M.; Disney, M.; Muller, J.P. Measuring forests with dual wavelength lidar: A simulation study over topography. *Agric. For. Meteorol.* **2012**, *161*, 123–133. [CrossRef]
20. Hancock, S.; Armston, J.; Hofton, M.; Sun, X.; Tang, H.; Duncanson, L.I.; Kellner, J.R.; Dubayah, R. The GEDI Simulator: A Large-Footprint Waveform Lidar Simulator for Calibration and Validation of Spaceborne Missions. *Earth Space Sci.* **2019**, *6*, 294–310. [CrossRef]
21. Hofton, M.A.; Minster, J.B.; Blair, J.B. Decomposition of laser altimeter waveforms. *IEEE Trans. Geosci. Remote Sens.* **2000**, *38*, 1989–1996. [CrossRef]
22. Hancock, S.; Lewis, P.; Disney, M.; Foster, M.; Muller, J.P. Assessing the Accuracy of Forest Height Estimation with Long Pulse Waveform Lidar Through Monte-Carlo Ray Tracing. In Proceedings of the Silvilaser, Edinburgh, UK, 17–19 September 2008; pp. 199–206.
23. Winker, D.M.; Couch, R.H.; McCormick, M. An overview of LITE: NASA's lidar in-space technology experiment. *Proc. IEEE* **1996**, *84*, 164–180. [CrossRef]
24. Schutz, B.E.; Zwally, H.J.; Shuman, C.A.; Hancock, D.; DiMarzio, J.P. Overview of the ICESat mission. *Geophys. Res. Lett.* **2005**, *32*. [CrossRef]
25. Winker, D.M.; Vaughan, M.A.; Omar, A.; Hu, Y.; Powell, K.A.; Liu, Z.; Hunt, W.H.; Young, S.A. Overview of the CALIPSO mission and CALIOP data processing algorithms. *J. Atmos. Ocean. Technol.* **2009**, *26*, 2310–2323. [CrossRef]
26. Stoffelen, A.; Marseille, G.; Bouttier, F.; Vasiljevic, D.; De Haan, S.; Cardinali, C. ADM-Aeolus Doppler wind lidar observing system simulation experiment. *Q. J. R. Meteorol. Soc. A J. Atmos. Sci. Appl. Meteorol. Phys. Oceanogr.* **2006**, *132*, 1927–1947. [CrossRef]
27. McGill, M.J.; Yorks, J.E.; Scott, V.S.; Kupchock, A.W.; Selmer, P.A. The Cloud-Aerosol Transport System (CATS): A technology demonstration on the International Space Station. In *Lidar Remote Sensing for Environmental Monitoring XV*; International Society for Optics and Photonics: Bellingham, WA, USA, 2015; Volume 9612, p. 96120A.
28. Stysley, P.R.; Coyle, D.B.; Kay, R.B.; Frederickson, R.; Poulios, D.; Cory, K.; Clarke, G. Long term performance of the High Output Maximum Efficiency Resonator (HOMER) laser for NASA's Global Ecosystem Dynamics Investigation (GEDI) lidar. *Opt. Laser Technol.* **2015**, *68*, 67–72. [CrossRef]
29. Konoplev, O.A.; Chiragh, F.L.; Vasilyev, A.A.; Edwards, R.; Stephen, M.A.; Troupaki, E.; Yu, A.W.; Krainak, M.A.; Sawruk, N.; Hovis, F.; et al. Three-year aging of prototype flight laser at 10 kHz and 1 ns pulses with external frequency doubler for ICESat-2 mission. In Proceedings of the Laser Technology for Defense and Security XII, Baltimore, MD, USA, 19–20 April 2016; Volume 9834, p. 98340A. [CrossRef]
30. Abshire, J.B.; Sun, X.; Mazarico, E.; Head III, J.W.; Yu, A.W.; Beck, J.D. A 3-D Surface Imaging Lidar for Mapping Mars and Other Bodies from Orbit. In Proceedings of the 51st Lunar and Planetary Science Conference, The Woodlands, TX, USA, 16–20 March 2020; p. 1966.
31. Kelemen, M.; Neukum, J. Semiconductor Tapered Amplifiers as a Tool for Quantum Technologies and LiDAR. *Coherent Webinar*. 2021. Available online: https://www.coherent.com/events/webinars (accessed on 4 April 2022).
32. European Thermodynamics Ltd. ET-071-10-13 Peltier Cooler Module. 2020. Available online: https://docs.rs-online.com/c588/0900766b8144a9b9.pdf (accessed on 4 April 2022).

33. Ziegler, M.; Hempel, M.; Larsen, H.E.; Tomm, J.W.; Andersen, P.E.; Clausen, S.; Elliott, S.N.; Elsaesser, T. Physical limits of semiconductor laser operation: A time-resolved analysis of catastrophic optical damage. *Appl. Phys. Lett.* **2010**, *97*, 10–13. [CrossRef]
34. Neuenschwander, A.; Pitts, K. The ATL08 land and vegetation product for the ICESat-2 Mission. *Remote Sens. Environ.* **2019**, *221*, 247–259. [CrossRef]
35. Yang, J.; Zhao, B.; Liu, B. Coherent Pulse-Compression Lidar Based on 90-Degree Optical Hybrid. *Sensors* **2019**, *19*, 4570. [CrossRef]
36. Sarwate, D.V.; Pursley, M.B. Crosscorrelation properties of pseudorandom and related sequences. *Proc. IEEE* **1980**, *68*, 593–619. [CrossRef]
37. Chu, D. Polyphase codes with good periodic correlation properties (corresp.). *IEEE Trans. Inf. Theory* **1972**, *18*, 531–532. [CrossRef]
38. Popovic, B. Generalized chirp-like polyphase sequences with optimum correlation properties. *IEEE Trans. Inf. Theory* **1992**, *38*, 1406–1409. [CrossRef]
39. Newnham, G.; Armston, J.; Muir, J.; Goodwin, N.; Tindall, D.; Culvenor, D.; Püschel, P.; Nyström, M.; Johansen, K. *Evaluation of Terrestrial Laser Scanners for Measuring Vegetation Structure*; CSIRO: Canberra, Australia, 2012.
40. Barton-Grimley, R.A.; Thayer, J.P.; Hayman, M. Nonlinear target count rate estimation in single-photon lidar due to first photon bias. *Opt. Lett.* **2019**, *44*, 1249–1252. [CrossRef] [PubMed]
41. Yang, G.; Martino, A.J.; Lu, W.; Cavanaugh, J.; Bock, M.; Krainak, M.A. IceSat-2 ATLAS photon-counting receiver: Initial on-orbit performance. In Proceedings of the Advanced Photon Counting Techniques XIII, Baltimore, MD, USA, 17–18 April 2019; International Society for Optics and Photonics: Bellingham, WA, USA, 2019; Volume 10978, p. 109780B.
42. Morimoto, K.; Charbon, E. High fill-factor miniaturized SPAD arrays with a guard-ring-sharing technique. *Opt. Express* **2020**, *28*, 13068–13080. [CrossRef] [PubMed]
43. Ito, K.; Otake, Y.; Kitano, Y.; Matsumoto, A.; Yamamoto, J.; Ogasahara, T.; Hiyama, H.; Naito, R.; Takeuchi, K.; Tada, T.; et al. A Back Illuminated 10 μm SPAD Pixel Array Comprising Full Trench Isolation and Cu-Cu Bonding with over 14% PDE at 940 nm. In Proceedings of the 2020 IEEE International Electron Devices Meeting (IEDM), San Francisco, CA, USA, 12–18 December 2020; IEEE: Piscataway, NJ, USA, 2020; pp. 16.6.1–16.6.4.
44. Kumagai, O.; Ohmachi, J.; Matsumura, M.; Yagi, S.; Tayu, K.; Amagawa, K.; Matsukawa, T.; Ozawa, O.; Hirono, D.; Shinozuka, Y.; et al. A 189 × 600 Back-Illuminated Stacked SPAD Direct Time-of-Flight Depth Sensor for Automotive LiDAR Systems. In Proceedings of the 2021 IEEE International Solid-State Circuits Conference (ISSCC), San Francisco, CA, USA, 13–22 February 2021; IEEE: Piscataway, NJ, USA, 2021; Volume 64, pp. 110–112.
45. Excelitas. SPCM-NIR: NIR-Optimized Single Photon Counting Module. 2020. Available online: https://www.excelitas.com/product/spcm-nir (accessed on 4 April 2022).
46. Giudice, A.; Ghioni, M.; Biasi, R.; Zappa, F.; Cova, S.; Maccagnani, P.; Gulinatti, A. High-rate photon counting and picosecond timing with silicon-SPAD based compact detector modules. *J. Mod. Opt.* **2007**, *54*, 225–237. [CrossRef]
47. Henderson, R.K.; Johnston, N.; Della Rocca, F.M.; Chen, H.; Li, D.D.U.; Hungerford, G.; Hirsch, R.; McLoskey, D.; Yip, P.; Birch, D.J. A 192 × 128 Time Correlated SPAD Image Sensor in 40-nm CMOS Technology. *IEEE J. Solid-State Circuits* **2019**, *54*, 1907–1916. [CrossRef]
48. Blair, J.B.; Hofton, M.A. Modeling laser altimeter return waveforms over complex vegetation using high-resolution elevation data. *Geophys. Res. Lett.* **1999**, *26*, 2509–2512. [CrossRef]
49. Duncanson, L.; Kellner, J.R.; Armston, J.; Dubayah, R.; Minor, D.M.; Hancock, S.; Healey, S.P.; Patterson, P.L.; Saarela, S.; Marselis, S.; et al. Aboveground biomass density models for NASA's Global Ecosystem Dynamics Investigation (GEDI) lidar mission. *Remote Sens. Environ.* **2022**, *270*, 112845. [CrossRef]
50. Hancock, S.; Anderson, K.; Disney, M.; Gaston, K.J. Measurement of fine-spatial-resolution 3D vegetation structure with airborne waveform lidar: Calibration and validation with voxelised terrestrial lidar. *Remote Sens. Environ.* **2017**, *188*, 37–50. [CrossRef]
51. Kahlig, P. Some aspects of Julius von Hann's contribution to modern climatology. *Geophys.-Monogr.-Am. Geophys. Union* **1993**, *75*, 1–7.
52. OpenTopography. *UMD-NASA Carbon Mapping/Sonoma County Vegetation Mapping and LiDAR Program*; OpenTopography: La Jolla, CA, USA, 2014. [CrossRef]
53. OpenTopography. *TEAM Lidar Data Over La Selva, Costa Rica 2009*; OpenTopography: La Jolla, CA, USA, 2019. [CrossRef]
54. National Ecological Observatory Network (NEON). *Elevation—LiDAR (DP3.30024.001)*; National Ecological Observatory Network (NEON): Boulder, CO, USA, 2021. [CrossRef]
55. TERN AusCover. FNQR Robson Creek—Airborne LiDAR Survey, 2012. Made Available by the AusCover Facility of the Terrestrial Ecosystem Research Network (TERN). Available online: http://www.auscover.org.au (accessed on 4 April 2022).
56. Neumann, T.A.; Brenner, A.; Hancock, D.; Robbins, J.; Saba, J.; Harbeck, K.; Gibbons, A.; Lee, J.; Luthcke, S.B.; Rebold, T.; et al. *ATLAS/ICESat-2 L2A Global Geolocated Photon Data, Version 4*; NSIDC NASA DAAC: National Snow and Ice Data Center: Boulder, CO, USA, 2021. [CrossRef]
57. Applied Research Laboratories. *PhoREAL, Version 3.24*; University of Texas: Austin, TX, USA, 2020.